Department of Physics and Astronomy
Heidelberg University

Bachelor Thesis in Physics
submitted by

Claudia Volk

born in Balingen (Germany)

2021

Excitation of the Secular Frequencies and Determination of the Operational Parameters of a Superconducting Radio Frequency Ion Trap by Laser-Power Modulation

This Bachelor Thesis has been carried out by Claudia Volk at the
Max-Planck-Institut für Kernphysik in Heidelberg
under the supervision of
Prof. Dr. José Ramón Crespo López-Urrutia

Abstract.

At the heart of the CryPTEx-II experiment at the Max-Planck-Institut für Kernphysik in Heidelberg is a superconducting radio frequency trap for simultaneous storage of highly charged ions together with a second species of laser cooled singly charged ions. During of this bachelor thesis, the trap parameters and the strength of the radio frequency field were determined. The secular frequencies of this superconducting quadrupole trap, in operation with singly ionized beryllium ions, were measured by means of motional excitation by an intensity-modulated cooling laser. The conversion of the nominally set DC parameters for axial storage to the potential inside the trap, as experienced by trapped ions, and a dependence of the pickup signal on the amplitude of the quadrupole field at the trap center were determined. The performed characterization aids in setting appropriate parameters for ion trapping and will benefit trap operation moving forward toward retrapping highly charged ions. In addition, the beam profile of the cooling laser in the trap center was investigated using simultaneous laser position and fluorescence measurements. For this purpose, a home-built motorized mirror mount, whose construction and first measurements will also be described here, was integrated into the laser setup. The demonstrated motorized mirror mount plus camera detector promises to be a broadly usable design for implementing computer-control and compensation of slow pointing drifts in laser setups.

Zusammenfassung.

Im Herzen des CryPTEx-II Experiments am Max-Planck-Instituts für Kernphysik in Heidelberg befindet sich eine supraleitende Radiofrequenzfalle zur simultanen Speicherung von hochgeladenen Ionen mit einer lasergekühlten zweiten Spezies von einfachgeladenen Ionen. Im Rahmen dieser Bachelorarbeit wurden aus den, mittels eines leistungsmodulierten Kühllasers vermessenen, Fallenfrequenzen dieser supraleitenden Quadrupolfalle, im Betrieb mit einfach ionisierten Berylliumionen, deren Fallenparameter und die Stärke des des Radiofrequenzfelds bestimmt. Die Umrechnung der eingestellten DC-Parameter zur axialen Speicherung auf das Potential im Innern der Falle, wie es von gefangenen Ionen erfahren wird, und eine Abhängigkeit vom Pickup-Signal zu der Amplitude des Quadrupolfelds im Fallenzentrum wurden ermittelt. Die durchgeführte Charakterisierung hilft bei der Einstellung geeigneter Parameter für den Ioneneinfang und wird den Fallenbetrieb in Richtung des Einfangens hochgeladener Ionen unterstützen. Zuden wurde das Strahlprofil des Kühlasers im Fallenzentum mittels gleichzeitiger Laserpositions- und Fluoreszenzmessung untersucht. Hierfür wurde ein selbstkonstruierter motorisierter Spiegelhalter, dessen Konstruktion und erster Vermessungen hier ebenfalls beschrieben werden sollen, in den Laseraufbau integriert. Die demonstrierte motorisierte Spiegelhalterung mit Kameradetektor verspricht, ein umfassend einsetzbares Design für die Implementierung von Computersteuerung und Kompensation von langsamen Pointing-Drifts in Laseraufbauten zu sein.

Contents

1 Introduction 1

2 Theoretical Background 3
- 2.1 The Paul Trap 3
  - 2.1.1 Ion Dynamics in the Ideal Paul Trap 4
  - 2.1.2 Micromotion 7
- 2.2 Laser Cooling 8
  - 2.2.1 Doppler Cooling 9
  - 2.2.2 Resolved Sideband Cooling 11
  - 2.2.3 Sympathetic Cooling 12

3 Experimental Setup of CryPTEx-II 13
- 3.1 The Trap Environment 13
  - 3.1.1 The Cryogenic Environment 13
  - 3.1.2 The Radio-Frequency Cavity 14
- 3.2 Laser Setup and Cooling 17
- 3.3 Imaging System and PMT 18

4 Development and Testing of a Motorised Mirror Mount 21
- 4.1 Design and Assembly 21
- 4.2 The First Test Setup 22

5 Characterisation of the Trap Parameters of CryPTEx-II 29
- 5.1 Secular Motion Excitation 29
- 5.2 Axial Secular Motion 30
- 5.3 Radial Secular Motion 34

6 Cooling Laser Profile in the Trap Centre 39
- 6.1 Incorporation of the MMM Into the Cooling Laser Setup 39
- 6.2 Calibration Using the DC Potential 40
- 6.3 Beam Width Measurements 44
  - 6.3.1 Measurements with the EMCCD camera 45
  - 6.3.2 Measurements with the PMT 47

7 Conclusion and outlook 51

Bibliography 55

1 Introduction

Spectroscopy has its beginnings in the 19th century with the discovery of the Fraunhofer absorption lines in the solar spectrum, and emitted light from different heated chemical elements which was resolved with a prism by Kirchhoff and Bunsen [1]. Since then it has helped shape our understanding of atoms, ions, and their interaction with light. The construction of the first lasers [2] helped to improve the precision that was possible with spectroscopy, for example with Doppler-free laser spectroscopy [3, 4] and laser cooling [5, 6]. Due to the reproducibility of atomic spectra in controlled environments, laser spectroscopy experiments quickly became the most precise preformed measurements.

Towards the end of the 20th century, the measurement of wavelengths became so accurate, that further improvement was only possible by measuring the frequency of light [7]. Very low systematic uncertainties of 3×10^{-18} [8] and 9.4×10^{-19} [9] have been reached for frequency measurements in single-ion clocks.

The search for new physics is an ongoing process and physics beyond the standard model can be probed in many ways. The most prominent experiments are performed with particle accelerators at high energies. On the other side of the spectrum are high precision experiments, performed by measuring the electric dipole moment of cold neutrons [10] — or frequency metrology with atoms or molecules.

Examples of such precision experiments, performed to search for physics beyond the standard model include Tests of QED [11] and local Lorentz-invariance [12], as well as the possible variation of fundamental constants, like the fine structure constant α or the proton-electron mass ratio [13]. A variance of the electromagnetic fine structure constant was suggested from astronomical data from a distant quasar [14] and has been attempted to be verified in measurements on earth.

The sensitivity of a transition depends strongly on the relativistic contribution of the involved energy levels. Since the overlap of the electronic wavefunction with the nucleus increases with higher charge states and charge number, transitions inside highly charged ions (HCIs) can obtain sensitivities by orders of magnitude larger than singly charged ions or atoms. Furthermore they have very narrow optical transitions that are less sensitive to external perturbations compared to atoms and ions currently used in atomic clocks [15]. This makes them a good candidate for more precise optical clocks and new frequency standards, and for probing fundamental physics. Over the time, they have been studied a lot less than their neutral or lowly charged counterparts (‘sea of ignorance’ [16], referring to the lesser amount of known electronic transitions in atomic systems with high ionic charge) because experiments with HCIs brings several challenges concerning their production, storage, and cooling.

HCIs can only be produced in high energy environments, which means they are initially very hot and not accessible for precision spectroscopy due to Doppler broadened spectral lines. For long time storage they need to be kept in an extremely high vacuum, otherwise they will lose their charge state via charge exchange reactions. Furthermore, they have no accessible transitions for laser cooling.

The cryogenic Paul trap experiment CryPTEx-II at the MPIK Heidelberg aims to perform quantum logic spectroscopy (QLS) with highly charged ions. A HCI will be trapped in an ion trap together with another ion, the logic ion, which has a fast closed cycle cooling transition. Due to the motional coupling inside the trap potential, this allows for sympathetic cooling of the HCI. After reaching the Lamb-Dicke regime, in modern experiments, the cooling ion, can be further utilized to read out the motional state of the spectroscopy ion to perform so called quantum logic spectroscopy [17]. The production of HCIs in this experiment is realised with an electron beam ion trap (EBIT), where an energetic electron beam ionises neutral atoms by electron impact ionisation to high charge states. In the EBIT the ions have temperatures in the megakelvin region, so the precision measurements will take part in a second ion trap, a linear Paul trap, were the ions can be stored for long periods of time under conditions suitable for precision spectroscopy. In the Paul trap, laser cooling can be applied to the logic ion species and the HCIs are sympathetically cooled alongside with them [18].

This work will focus on the linear Paul trap, where the QLS with retrapped HCIs will take place in the future, and the laser systems surrounding it. To characterize the trapping potentials and find appropriate settings for ion trapping, the motion of singly charged beryllium ions was used to determine the characteristic trap parameters. The fluorescence of the beryllium ion was used to study the focus of the Doppler cooling beam in the trap centre to understand the interaction between the ions and the laser system. For this, a new computer-controlled mirror mount was developed together with a camera based system for detecting the laser spot position for improved and reproducible laser pointing control.

2 Theoretical Background

This chapter introduces the theoretical basis for the measurements and their evaluation conducted in this work. Section 2.1 gives an overview of the working principle of a linear Paul trap. Afterwards, in Section 2.2 laser cooling is discussed.

2.1 The Paul Trap

As discussed in Chapter 1 the work with confined ions is an essential part of atomic physics. They have limited motion and can potentially be cooled down by several orders of magnitude compared to free ions which makes them available for very precise measurements [19].

According to Earnshaw's theorem, it is not possible to use only static electric fields to generate a three-dimensional potential well, i.e. such fields cannot result in a stable equilibrium state [20]. Several kinds of traps exist that offer different solutions to this problem, the two main kinds of ion traps that are typically used are Penning traps and Paul traps. While Penning traps use magnetic fields as a principal trapping element in addition to static electric fields [21], in Paul traps there are time-dependent alternating electric fields, in the radiofrequency regime in particular [22]. This work focuses on the latter.

Paul traps, sometimes also called radio frequency (rf) traps or quadrupole ion traps were invented by Wolfgang Paul [23]. They use dynamic rf electric fields to store charged particles radially and a static potential for axial confinement, in the case of linear Paul traps. The name quadrupole ion trap refers to the radial electric field geometry. Even though several different types of trap electrodes can be used to generate such a quadrupole field and an additional static axial field, mostly a linear build is preferred. Here there are four (or more) rod shaped electrodes (circular or hyperbolic) arranged parallel to each other and the trap axis, in a square configuration around the axis.

In this work the trap axis, perpendicular to the quadrupole field, is denoted as the z axis, and the two axes of the quadrupole are denoted x and y.

For the description of the dynamics in the ideal Paul trap, a perfect radial quadrupole field and axial harmonic field are assumed, as they would be produced by a perfect electrode geometry (that is, perfectly hyperbolical, infinitely long).

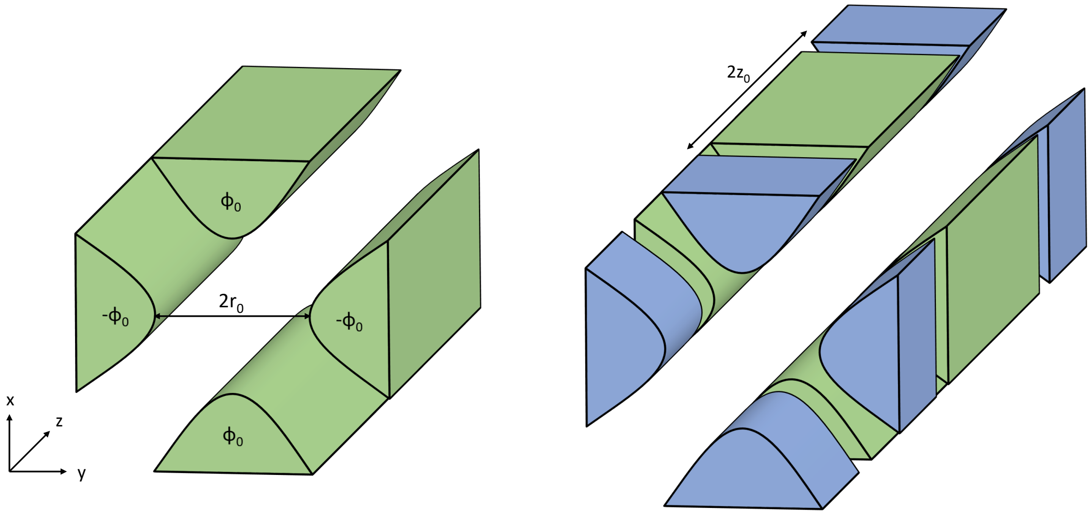

(a)

(b)

Figure 2.1: Schematic picture of a possible set of Paul trap electrodes. **(a)** 4 hyperbolic electrodes with opposite electrodes on the same and neighbouring electrodes on reversed potential $\pm\phi_0$ generate a quadrupole field along the trap axis. They each are a distance of r_0 from the trap axis. **(b)** A three dimensional Paul trap has, besides the hyperbolic rf electrodes (green), additional DC electrodes (blue). Such a set-up, with 8 elements which are in the shape of quadrupole electodes, is shown. The DC electrodes are separated by $2z_0$ and supply the axial static potential.

2.1.1 Ion Dynamics in the Ideal Paul Trap

The introduction to the working principle of a Paul trap that is presented in this subsection is based on [22, 24].

As mentioned above, the radial confinement is realised via a rf electric field. A quadrupole field can be generated by four hyperbolic electrodes, with opposite electrodes on the same potential and neighbouring electrodes on opposite potentials. Such an arrangement can be seen in Figure 2.1a. The potential of the linear Paul trap is then

$$\phi(\boldsymbol{x}, t) = \phi_0(t)\,\frac{x^2 - y^2}{r_0^2}, \tag{2.1}$$

where r_0 is the distance from each electrode to the trap axis. $\pm\,\phi_0(t)$ is the potential of the electrodes along x- and y-axis, respectively. When $\phi_0(t)$ is positive, the resulting electric field can trap a positively charged particle in x direction, but not in y direction, such a quadrupole potential is shown in Figure 2.2a

For a linear Paul trap we choose $\phi_0(t)$ as an oscillation with radio frequency Ω, amplitude

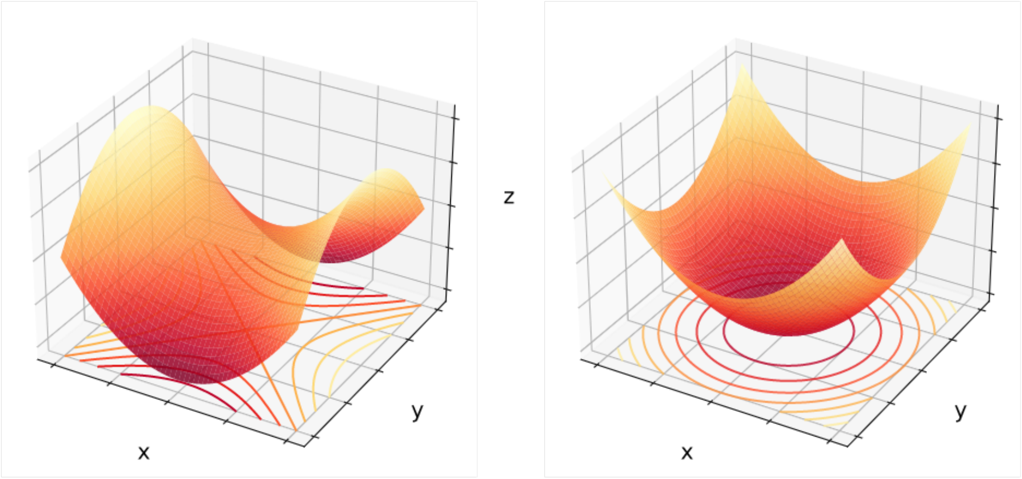

(a) (b)

Figure 2.2: **(a)** Quadrupole-potential at a particular time t. For a positive ion, confinement is given in y direction but not in x direction. **(b)** An ion with a stable solution experiences a pseudo potential averaged over time.

V and offset U_r, this gives

$$\phi_0(t) = V\cos(\Omega t) + U_r. \tag{2.2}$$

As a result, a charged particle is alternately confined in x and y direction. The trap frequency Ω can be chosen in such a way that a charged particle has a stable trajectory and, averaged over time, experiences a pseudo potential well in both x and y directions, as seen in Figure 2.2b.

For a particle of mass m and charge Q we have classically

$$\ddot{\boldsymbol{x}} = \frac{\boldsymbol{F}}{m} = -\frac{Q}{m}\boldsymbol{E} = -\frac{Q}{m}\nabla\phi(t), \tag{2.3}$$

which leads to the following equations of motion in the potential of Equation (2.1)

$$\begin{aligned} \ddot{x} &= -\frac{Q}{m}\,\partial_x\phi(t) = -\frac{2Q}{mr_0^2}\,(V\cos(\Omega t) + U_r)\;x, \\ \ddot{y} &= -\frac{Q}{m}\,\partial_y\phi(t) = +\frac{2Q}{mr_0^2}\,(V\cos(\Omega t) + U_r)\;y, \\ \ddot{z} &= 0. \end{aligned} \tag{2.4}$$

The part still missing from the model so far is the confinement along the z axis, the trap axis. For this, a static electric field with a potential of the form

$$\phi_z = \frac{\kappa U_z}{z_0^2}\left(z^2 - \frac{x^2}{2} - \frac{y^2}{2}\right) \tag{2.5}$$

is applied with additional electrodes, the DC electrodes, with a distance of z_0 from the trap centre and an applied voltage of U_z. They can have different kinds of geometries, one example is shown in Figure 2.1b, where four DC electrodes that have the same shape as the quadrupole electrodes are placed on either side of the trap centre. $\kappa < 1$ is a geometrical factor, depending on the chosen shape of the DC electrodes.

The equations of motion become

$$\ddot{x} = -\frac{2Q}{m}\left(\frac{V\cos(\Omega t)}{r_0^2} + \frac{U_r}{r_0^2} - \frac{\kappa U_z}{2z_0^2}\right)x, \tag{2.6}$$

$$\ddot{y} = -\frac{2Q}{m}\left(-\frac{V\cos(\Omega t)}{r_0^2} - \frac{U_r}{r_0^2} - \frac{\kappa U_z}{2z_0^2}\right)y, \tag{2.7}$$

$$\ddot{z} = -\frac{2Q}{m}\frac{\kappa U_z}{z_0^2}\,z\,. \tag{2.8}$$

Defining the dimensionless a and q parameters,

$$a_{x,y} = \frac{4Q}{m\Omega^2}\left(\pm\frac{2U_r}{r_0^2} - \frac{\kappa U_z}{z_0^2}\right), \qquad a_z = \frac{8Q\kappa U_z}{m\Omega^2 z_0^2}, \tag{2.9}$$

$$q_{x,y} = \mp\frac{4QV}{mr_0^2\Omega^2}, \qquad q_z = 0\,, \tag{2.10}$$

we can simplify the equations of motion as

$$\ddot{u} + \frac{\Omega^2}{4}\left(a_u - 2q_u\cos(\Omega t)\right)u = 0, \qquad \text{with } u = \{x, y, z\}\,. \tag{2.11}$$

These kinds of differential equations are called Mathieu equations [25]. They have two types of solutions; they can be either stable, where $u(t)$ has a closed trajectory and is bounded for $t \to \infty$, or instable, where $u(t)$ grows exponentially. If x, y, z are all stable, the ion can be trapped indefinitely for an ideal trap.

With the general solution of the Mathieu equations one can find stability regions of the x- and y-component for certain values of a_x and q_x, and for vanishing axial potential. They are shown in Figure 2.3.

Due to the complexity of the general solution, only an approximation of a certain class of stable solutions will be discussed in the following. The most commonly used approximation to describe the motion in a Paul trap is the so called adiabatic approximation where

$$|a_u| \ll q_u \ll 1, \qquad \text{for } u = x, y, z, \tag{2.12}$$

holds. In the stability diagram in Figure 2.3 this would be found in the part of the yellow region close to the origin. In this approximation, the solution of the Mathieu equation becomes

$$u(t) = u_0\cos(\omega_u t)\left(1 + \frac{q_u}{2}\cos(\Omega t)\right), \tag{2.13}$$

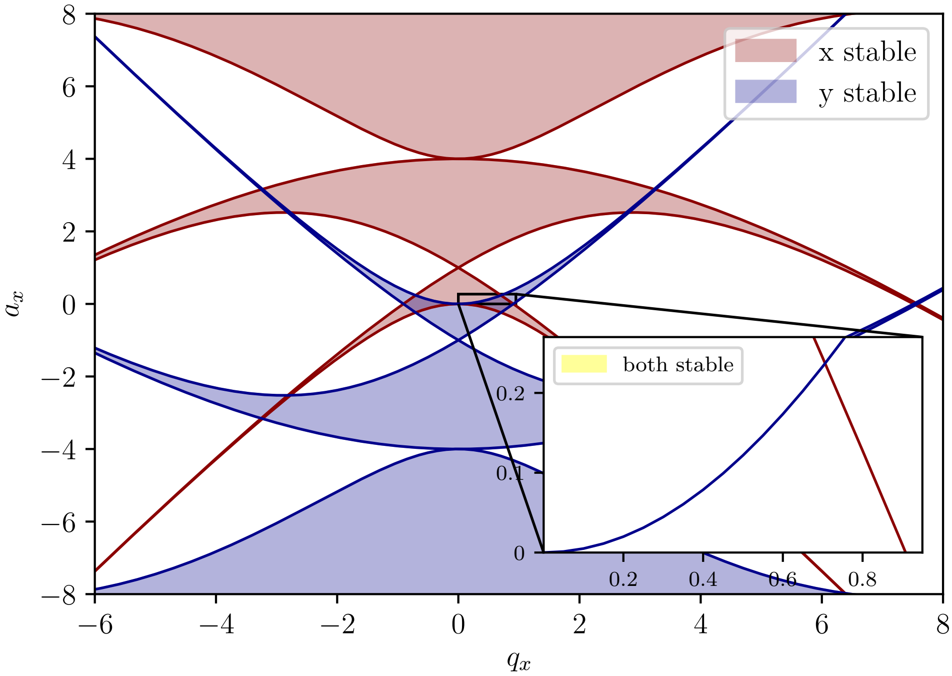

Figure 2.3: Stability diagram following from the Mathieu equation for the radial motion depending on $a_x = -a_y$ and $q_x = -q_y$, as defined in Equation (2.9) and Equation (2.10), with no axial confinement $U_z = 0$. The areas shaded in red (blue) indicate solutions where an ion is bounded in x (y) direction, the yellow region indicates the typical trapping region of a Paul trap where both radial components yield stable solutions.

where ω_u, called the secular frequency, is given by

$$\omega_u = \frac{\Omega}{2}\sqrt{a_u + \frac{q_u^2}{2}}\,. \tag{2.14}$$

The solution in Equation (2.13) splits into a macromotion or secular motion, the first term, with frequency ω_u, and a micromotion at the trap frequency Ω, the second term in the equation, which will be discussed in the next subsection. For the axial motion the micromotion term in Equation (2.13) vanishes because $q_z = 0$.

2.1.2 Micromotion

In the previous Section, in Equation (2.13), we saw that the ion motion is not only dictated by the secular motion, but that there is a faster, intrinsic micromotion and the trap frequency Ω as well. Further micromotion, not caused by the ideal trap potential itself, can be present in an rf ion trap.

The main causes of additional micromotion will be briefly discussed here. A more in depth exploration of different kinds of micromotion and their effect on the ion motion can be found in [26].

An additional static electric field, which can be caused by depositions on the electrodes or a radial imbalance of the supplied DC potential for axial confinement, causes a shift in the ion position. Equation (2.13) becomes [26]

$$u(t) = (\widetilde{u}_0 + \widetilde{u}_1 \cos(\omega_u t)) \left(1 + \frac{q_u}{2} \cos(\Omega t)\right), \tag{2.15}$$

and the additional term $\widetilde{u}_0$ causes an offset in the average ion position as well as an additional term in the micromotion of amplitude $\widetilde{u}_0 q_u/2$, while the secular motion stays the same. This extra motion is driven by the rf field, and cannot be lowered via laser cooling.

A phase shift $\Delta\phi$ in the AC supply for one of the opposite rf electrode pairs can also lead to excess micromotion. For a potential of the form $V\cos(\Omega t \pm \Delta\phi)$, additional electric fields are induced and interact with a trapped ion. Similar to the first discussed case, this results in additional micromotion; in the lowest order this will again be in radial direction and as before it is not thermal motion that can be laser cooled.

Lastly, a difference in rf amplitude of the two electrode pairs causes micromotion in all directions, radial and axial. The exact effect needs to be studied with simulations, for instance seen in [27].

When experimenting with a Paul trap the goal is to lessen all potential causes of excess micromotion as much as possible since it can generally not be laser cooled. Therefore, good understanding of the trap potentials is reqiured. For precision spectroscopy it is essential to minimise ion motion to reduce Doppler broadening of transitions, and for quantum logic spectroscopy (QLS) cooling to the motional ground state is a necessity.

2.2 Laser Cooling

To minimise the ion motion in a trap it is desirable to have the ions be as cold as possible. This decreases the Doppler broadening of spectral lines and makes more precise measurements possible. Since the trapped ions will not be in thermal contact to their environment, one needs to apply direct cooling, which is done in the form of laser cooling. Perhaps somewhat counterintuitively, various techniques exist where a strong light source such as a laser is used to reduce motional excitations of an atom through photon-induced transitions, thereby reducing its motion and its temperature. Here discussed is the most widely used laser cooling method, Doppler cooling, afterwards the technique of sympathetic cooling is described.

2.2.1 Doppler Cooling

This form of laser cooling can cool the motion of ions and atoms down to their so called Doppler limit. It uses a closed, fast decaying transition in the atomic structure and the momentum transfer that is caused by absorption or emission of photons. This section will describe the cooling of ions, though this method can be similarly applied to atoms with a fitting atomic transition.

In order to be suitable for Laser cooling, the ion species of interest requires a fast decaying excited state that forms a closed transition with a lower energy state and has a laser accessible energy difference. The condition of a short-lived excited states results in dipole-allowed transitions being suitable for Doppler cooling and a transition being closed indicates that the excited state can only decay into the initial ground state and not into a possible third state.

When a photon with the relevant energy difference hits the ion, it can be absorbed and the momentum of the ion will change along the propagation direction of the light according to the photon momentum,

$$\boldsymbol{p_\gamma} = \hbar \boldsymbol{k}, \tag{2.16}$$

where $k = 2\pi/\lambda$ is the wavenumber, due to momentum conservation. For the same reason the ion regains the absolute value of the momentum once it falls back to the ground state and emits a photon. However, this is an isotropic process for dipole transitions and the gained momentum has a random direction. Utilising a fast decaying excited state with a closed transition, this happens very quickly and repeatedly. Since the emission process is isotropic and the absorbed photons are from a directed light field, there is a finite momentum transfer in the direction of the light field over many absorption-emission cycles. For a laser that has been red tuned by Δ with respect to the transition frequency ω_e ($\omega_{\text{laser}} = \omega_e - \Delta$), the Doppler effect causes absorption to be more likely for ions moving towards the laser beam, slowing them down.

To lower the overall motion of a particle, i.e. its temperature, one can apply six such lasers, two counter-propagating beams for each spatial dimension. This inspires the construction of another kind of particle trap, the magneto-optical trap[28]. For an ion trapped by other means, e.g. a Paul trap, one laser beam is sufficient given that it couples to all three motional degrees of freedom in the trap [29].

For a more quantitative approach we look at the case of an ion in a Paul trap where we assume it moves in the pseudopotential according to the secular motion and neglect the micromotion. This is discussed in more detail in [30].

The ion will be approximated as a two-level-system with a ground state $|g\rangle$ and one excited state $|e\rangle$. The lifetime of the excited state will be assumed to be much shorter than an oscillation period in the trap potential which means that the ion does not significantly change its velocity during an absorption-emission cycle. The process can therefore be treated the same as for a free ion with a certain velocity v.

The product of the decay rate Γ and the probability of the ion to be in the excited state ρ_{ee} determines the rate of the absorption-emission cycles. With Equation (2.16) the force onto the ion per absorbed photon is given by

$$F_\gamma \simeq p_\gamma \, \Gamma \, \rho_{ee} = \hbar \, k \, \Gamma \, \rho_{ee}. \tag{2.17}$$

With the saturation parameter of the transition,

$$s = \frac{2|\Omega_\mathrm{R}|^2}{\Gamma^2} = \frac{I_s}{I}, \tag{2.18}$$

that can either be expressed via the Rabi frequency Ω_R of the laser and saturation intensities I_s and I, respectively, the probability ρ_{ee} can be expressed as

$$\rho_{ee} = \frac{s/2}{1 + s + (2\delta_\mathrm{eff}/\Gamma)^2}\,. \tag{2.19}$$

The effective detuning $\delta_\mathrm{eff} = \Delta - \boldsymbol{k}\cdot\boldsymbol{v}$ is the shift from the transition frequency the ion sees, taking both the Doppler shift caused by the ion's velocity and the detuning of the laser into account.

For small velocities $\boldsymbol{k}\cdot\boldsymbol{v} \ll \Delta$, F_γ can be linearised in v, to

$$F_\gamma \approx \underbrace{\hbar k \Gamma \frac{s/2}{1 + s + (2\Delta/\Gamma)^2}}_{F_0} (1 + \alpha v) \qquad \text{with } \alpha = \frac{8k\Delta/\Gamma^2}{1 + s + (2\Delta/\Gamma)^2}\,. \tag{2.20}$$

Averaged over many absorption-emission cycles a cooling rate can be derived from F_γ. However, an ion can never be cooled down to zero velocity , as it will always absorb and emit photons where the emission, it being isotropic, leads to a random walk in momentum space about some point. This leads to diffusion and gives rise to a heating rate. Therefore, the cooling limit, called the Doppler limit, is reached when these heating and cooling rates are equal.

If one neglects the correlation between absorption and emission rates, which is a good approximation for a weakly driven cooling transition ($s \ll 1$), the Doppler limit is given as

$$T_\mathrm{Doppler} = \frac{\hbar\Gamma\sqrt{1+s}}{4k_B}\,(1+\beta). \tag{2.21}$$

It is typically of the order of mK; for Be$^+$, which is the relevant ion species in this work, it is $T_\mathrm{Doppler} = 302\,\mu\mathrm{K}$ [31]. The Doppler limit is reached for a detuning of

$$\Delta = \frac{\Gamma\sqrt{1+s}}{2}\,. \tag{2.22}$$

The geometric factor β is needed to account for the scaling between absorption and emission because the absorption is directed along the laser field and emission is isotropic. For a dipole transition $\beta = 2/5$ [32].

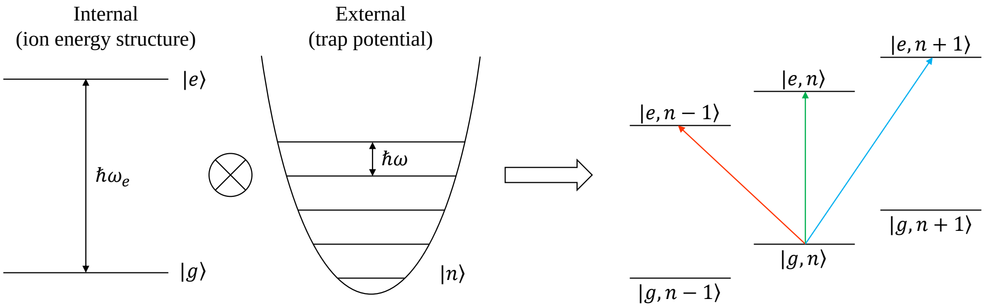

Figure 2.4: Schematic picture of the states of a two-state system coupled with an external harmonic oscillator. Within the resulting energy states on the right hand side are several possible transitions, including those that change the motional quantum number n, thereby producing sidebands in the spectrum, equidistant from the central excitation frequency ω_e. The sidebands can only be resolved if the linewidth of the transition is much smaller than the HO frequency ω, $\Gamma \ll \omega$.

2.2.2 Resolved Sideband Cooling

To cool ions below their Doppler limit further cooling methods need to be employed. One such method is called resolved sideband cooling [30] which will be used in our experiment. A brief overview of this method is given here.

The quantum state of an ion trapped in a harmonic potential is described by the combination of internal state, according to the internal electronic energy levels and an external motional state, a Quantum Harmonic Oscillator (QHO) state. The resulting level structure and the transitions give rise to sidebands on the electronic transitions as pictured in Figure 2.4.

The further cooled down the ion gets, the less Doppler broadened the line shapes of the ions are, and the more resolved the sidebands become. The degree to which sidebands are resolved also depends on the natural width of the transition and on their distance from the central line which corresponds to the harmonic oscillator frequency. Hence, a reasonably large trapping frequency, the one characterising the QHO which in a Paul trap corresponds to the secular frequency ω_u, and a narrow natural linewidth are needed. Dipole forbidden transitions or Raman transitions are typically used here [30].

In the Lamb-Dicke regime, where transitions including more than one phonon (a quantum of motion in the external potential) are suppressed, resolved sideband cooling can be employed. The Lamb-Dicke parameter η is defined as $\eta = kz_0 = 2\pi z_0/\lambda$, the ratio of the expansion of the wavepacket of the ion in the vibrational ground state z_0 and the wavelength of the transition λ. The condition to be in the Lamb-Dicke regime is described with the Lamb-Dicke parameter and the motional quantum number n as $\eta^2(2n+1) \ll 1$, where the expansion of the wavefunction is much smaller than the wavelength. The coupling strengths of the sidebands depend on the parameter η, so the greater the number of changed motional quantum number, the more suppressed the transition becomes in the Lamb-Dicke regime.

An incoming laser beam at the excitation frequency ω_e is red tuned according to the trapping frequency ω and can therefore lift an ion into the exited state of the next lower motional mode. The excited state is most likely going to decay into the ground state with no change in motional quantum number.Due to the equidistant spacing of the QHO states this can be repeated until the probability of being in the motional ground state $|n = 0\rangle$ is very high.

2.2.3 Sympathetic Cooling

The goal of the experiment is to perform quantum logic spectroscopy on HCIs for which they need to be cold. Since the HCIs typically do not have laser accessible closed-cycle transitions — at least with commercially available lasers — that can be used for Doppler cooling, they need to be cooled down by other means. A possible solution in the simultaneous trapping of a second ion species that can be Doppler cooled. Through the Coulomb interaction between the ions they share motional modes and cooling one class of ions will lower the other's thermal motion as well. This is called sympathetic cooling, first demonstrated in Ref. [33].

For this to work the trap must allow for the HCI and a second class of ion, here singly charged beryllium ions, to be trapped together. In a Paul trap this can be achieved for ions that have similar charge to mass ratio, as the equations of motion Equations (2.6) to (2.8) will be similar and the stability parameters for both species are in the stability region. This has been done in Ref. [18] for instance.

3 Experimental Setup of CryPTEx-II

The work for this thesis was conducted as part of the cryogenic Paul trap experiment CryPTEx-II at the MPIK Heidelberg. Its predecessor is CryPTEx [34] from which the biggest difference is the superconducting rf cavity, constructed almost entirely of niobium.

The complete experimental setup can be seen in Figure 3.1. Here the relevant components of the experimental setup are introduced and explained, the exact construction and more details can be found in Ref. [31].

First the trap environment will be introduced in Section 3.1, then the laser systems in use will be explained in Section 3.2 and lastly we will talk about the imaging system in Section 3.3.

3.1 The Trap Environment

At the centre of CryPTEx-II is a combination of a linear Paul trap and a superconducting rf cavity where the superconducting cavity supplies the rf quadrupole field for radial confinement. The trap is placed inside a cryogenically cooled environment that has two temperature stages at 40 K and 4 K. The cryogenic environments are set inside a vacuum chamber where we have an extremely high vacuum which is crucial for precision work with HCIs as these would otherwise be lost in charge-exchange reactions.

3.1.1 The Cryogenic Environment

As seen in Figure 3.2, two temperature stages make up the cryogenic environment.

The trap itself is cooled down to 4 K and this 4 K region (the second stage) is enclosed in a 40 K temperature shield (the first stage). Cooling the trap is necessary to bring the superconducting resonator below its critical temperature of 9.25 K [35]. Such a low temperature also decreases the overall vacuum to as low as the upper 10^{-10} mbar range [31]. Inside the 4 K stage it could be even lower, by freezing out many of the residual gas atoms and molecules. This reduced the possibility of charge exchange processes and collisions with other particles and improves the lifetime of the ions in the trap.

Inside the vacuum chamber is the region at 40 K to shield and reduce the thermal load on the second stage at 4 K. This first stage blocks the second stage from the thermal radiation of the surrounding room temperature vacuum setup and hence decreases the cooling power needed to maintain the ideal trap temperature.

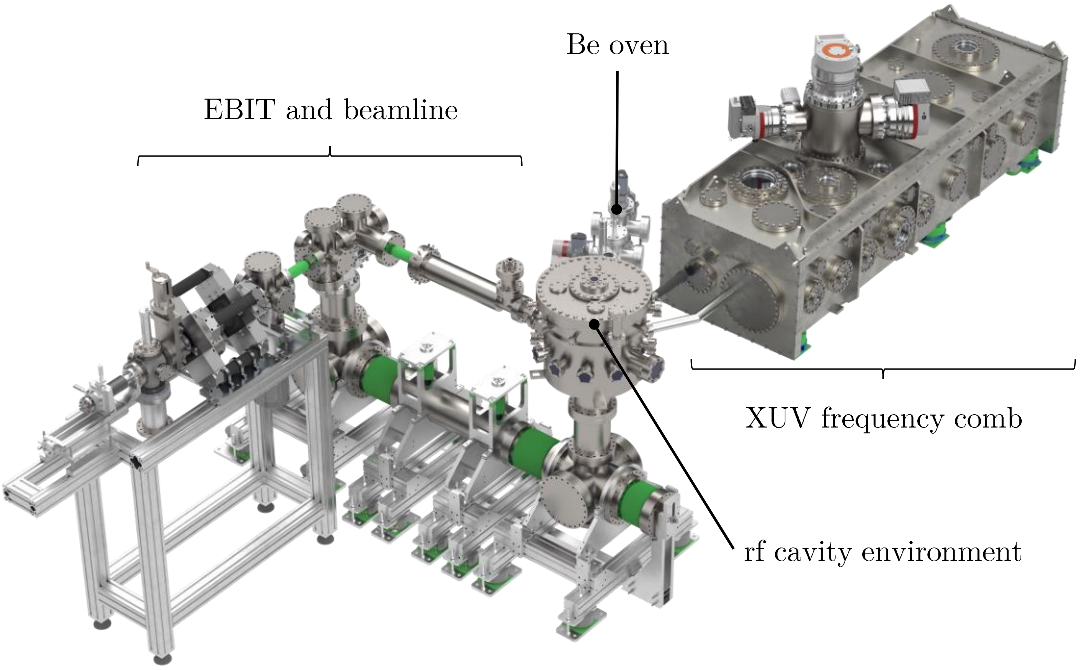

Figure 3.1: Overview of the eventual CryPTEx-II experiment, including the EBIT and beamline as a HCI source, the Be oven for the Be$^+$ production, and the XUV frequency comb for precision spectroscopy. The latter is not yet installed at the shown position at the time of this work. At the centre the vacuum chamber for the rf cavity can be seen. Figure with adjustments taken from Ref. [31].

An essential feature for a setup designed to perform high-precision spectroscopy, is that external vibrations have to be as decoupled as possible to prevent motional heating of the ions. Major sources of external vibrations include parts of the experimental setup: the vacuum pumps, like scroll pumps and turbo-molecular pumps and the cryo-cooler, as well as general vibrational noise from the laboratory, like from the air-conditioning, vibrations of the floor etc. The former are reduced by separating these vibration-inducing machines from the trap setup itself by assembling them in different rooms. They are connected through the wall by a thermal transport unit that can be seen in Figure 3.2 which decouples a large degree of vibrations [36].

3.1.2 The Radio-Frequency Cavity

The quadrupole resonator that makes up the main part of CryPTEx-II is a combination of a resonator cavity with a linear Paul Trap. It is able to produce a very stable rf potential for trapping the ions.

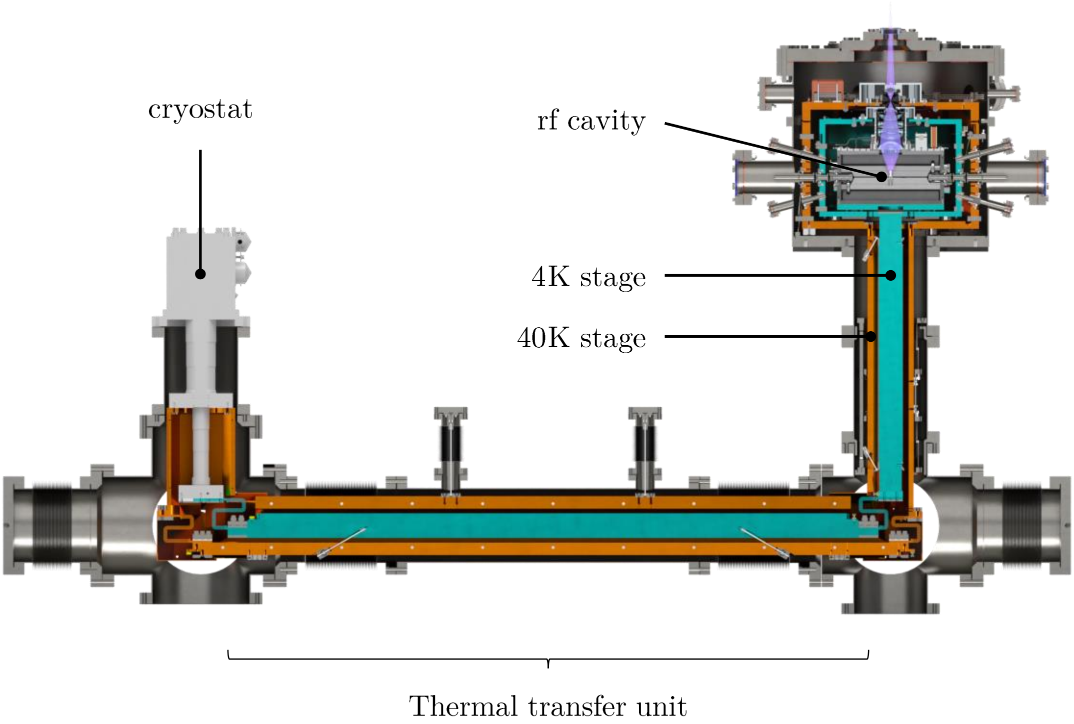

Figure 3.2: The cyogenic setup, consisting of the first stage at 40 K and the second stage at 4 K can be seen. The cryostat in the neighbouring laboratory is thermally connected to the cryogenic trap environment via the vibration decoupling thermal transfer unit. The resonator is mounted to the 4 K stage and hereby brought below its critical temperature. Figure with adjustments taken from Ref. [31].

A cavity resonator acts as a narrow band-pass filter at its resonant frequency Ω, which means electrical noise is highly suppressed [31]. The cavity at the heart of CryPTEx-II is made out of superconducting niobium, this reduces electrical losses inside the cavity and improves the quality factor of the band-pass. Consequently, the trapping conditions for the ions are able to become extremely stable.

The trap electrodes inside the cavity can be seen in Figure 3.3. The electrodes are tilted by 45° relative to the x and y axes as they were defined in Section 2.1, to allow optical access. They are connected to the cavity itself on one side each in a quadrupole configuration. Each electrode has an outer and an inner part where the potentials are opposite, i.e. they are connected to opposite sides of the cavity. This configuration leads to a relatively large capacity for a resonator of these dimensions resulting in a lower resonance frequency, meaning the same radial q values can be reached with a smaller rf amplitude V (compare Equation (2.10)). The electrodes are not perfectly hyperbolic but are slightly altered to allow a better optical access to the trap centre.

Eight DC electrodes are fixed in the quadrupole electrodes with a distance of z_0 =

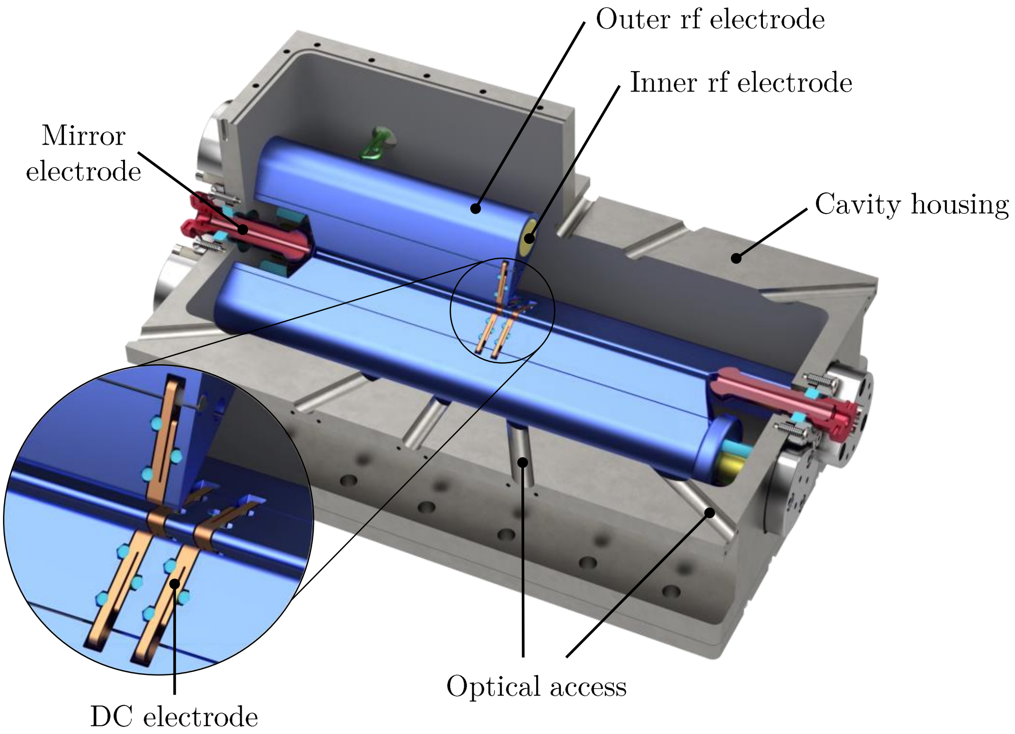

Figure 3.3: Pictured is the rf cavity with its different electrodes. The rf quadrupole electrodes are mounted to the cavity and are made up of and inner and an outer part. The two mirror electrodes, needed for HCI retrapping, are situated along the trap axis on either end of the cavity. The DC electrodes can be seen in more detail in the inset. Figure with adjustments taken from Ref. [31].

2.05 mm from the trap centre. The voltage for each of them can be individually set, meaning it can be used to minimise micromotion due to misalignment of rf and DC minimum. In addition to the set voltage, the DC electrodes also carry the same rf voltage as the quadrupole electrode they are set into, as being so close together capacitively couples them.

The trap centre needs to be accessed from the outside for laser cooling and loading ions into the trap, with lasers and atomic/ion beams, respectively. For this reason 12 optical ports in the horizontal plane at the height of the trap centre are included in the cavity, 30° apart each. Figure 3.5 shows the optical ports and their assignment at the time of this thesis. Additional to the horizontal ports, there is access on the top of the cavity where the imaging system collects the fluorescence light of the ions, more on this in Section 3.3.

3.2 Laser Setup and Cooling

The two laser systems in use at the time of this thesis will be described in the following.

First, there is the photoionisation (PI) Laser system to ionise Be atoms to Be^+ which can then be trapped. The ionisation energy of beryllium is 9.32 eV [37] which corresponds to a wavelength of 133 nm. The production of such laser wavelengths is very challenging, and additionally such wavelengths would be absorbed by the air the light propagates through which can produce ozone. Therefore the atoms get ionised with two photons in total via an intermediate excited state with a dipole allowed transition of 235 nm. From there, the absorption of a second photon with the same energy ionised the beryllium.

The laser light of 235 nm is produced in two steps from a 940 nm laser. It is frequency doubled twice, first with a PPKTP (periodically poled potassium titanyl phosphate) crystal to 470 nm and a second time to the desired 235 nm using a BBO (beta barium borate) crystal [38].

The setup for this laser is placed in a laboratory a floor below the one housing the rf cavity. So the generated PI laser light has to be guided through the floor (or ceiling, depending on the point of view) through several pipes to reach the trap. Beam stabilising piezo-driven mirrors are employed to account for beam position fluctuations over the long distance. After being directed into the trap the PI laser beam hits the atomic beam in the centre at an angle of 90° to minimise the Doppler effect due to the beam velocity.

The second laser system is the one used for Doppler cooling (see Section 2.2.1) the beryllium ions in the trap. A singly charged beryllium ion has 3 electrons, 2 in the 1s shell and one in the 2s shell, in case of the ground state configuration. The closed first shell is inaccessible with the lasers we use, so effectively this can be treated as a one-electron system.

The single valence electron has a transition of 313 nm from the ground state $2S_{1/2}$ into the $2P_{3/2}$ state, which is used for Doppler cooling [39]. This is a very fast-decaying transition but it is not a closed cycle, as the ground state has a hyperfine splitting of 1.25 GHz into $F = 1$ and $F = 2$ due to the nuclear spin [39]. To close the transition, a repumper laser is needed to depopulate the upper hyperfine state to ensure efficient cooling. Figure 3.4 shows the relevant transitions and levels of Be^+ for the laser cooling.

The 313 nm light is supplied by a commercial UV laser system[1] where it is produced by frequency doubling a diode laser twice. The necessary repumper laser is realised by sampling a fraction of the laser light — typically about 15 % — with a beam splitter and adjusting its frequency to give the cooling laser beam and the repumper a frequency difference of 1.25 GHz according to the hyperfine splitting.

This frequency shift is realised with the use of several acusto-optic modulators (AOM). The repumper beam passes through two AOMs that have 200 MHz and 425 MHz. It

---

[1] TOPTICA Photonics AG TA-FHG pro

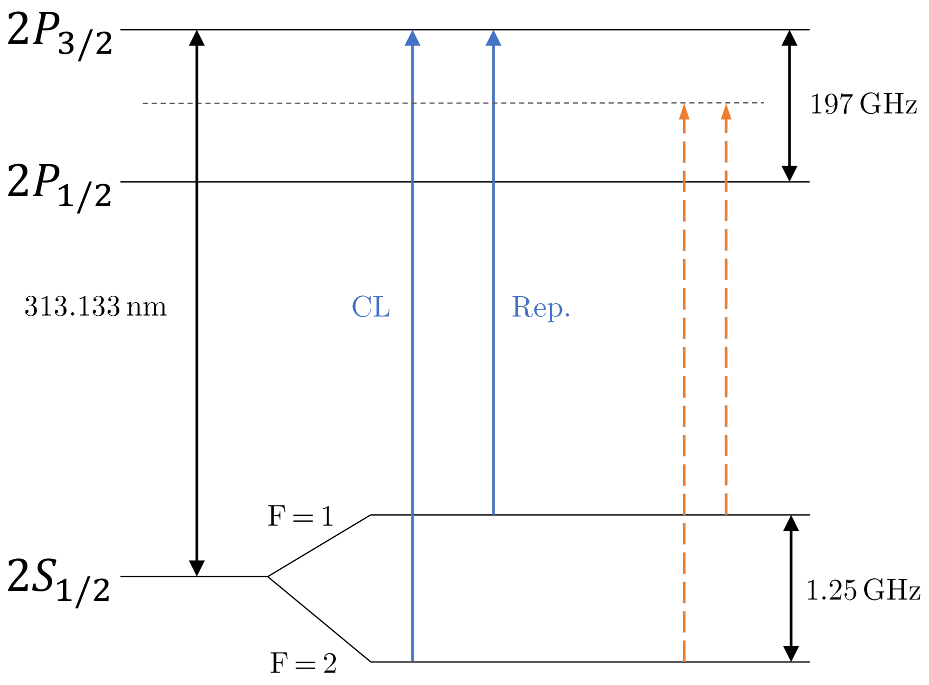

Figure 3.4: The for the laser cooling essential energy levels of Be$^+$ (not to scale). In blue it shows the transitions for the cooling laser (CL) and the repumper (Rep.), indicated in orange is the Raman transition that will be used for resolved sideband cooling in the future.

goes through the first one once, in the -1^{st} order and through the second one twice, again both times in the -1^{st} order. The last 200 MHz that are missing to the 1.25 GHz difference is accounted for with the cooling laser frequency. The cooling laser beam passes trough an AOM with 200 MHz in the $+1^{\text{st}}$ order. Additionally, this can be used to power stabilise the cooling laser, and it can be used to excite the motional modes of trapped ions by modulating the intensity with the secular frequencies.

Figure 3.5 shows the essential parts of the two laser setups.

3.3 Imaging System and PMT

The imaging setup collecting the emitted fluorescence light from trapped ions, pictured in Figure 3.6, is installed on top of the cavity. This system was developed in Ref. [40] to collect the fluorescence photons as efficiently as possible. A stack of lenses is fixed directly on the cavity at the 4 K stage, preventing misalignment during cooldown. It accumulates the light from the trap centre, reaching an efficiency of 3.45 %, and focuses

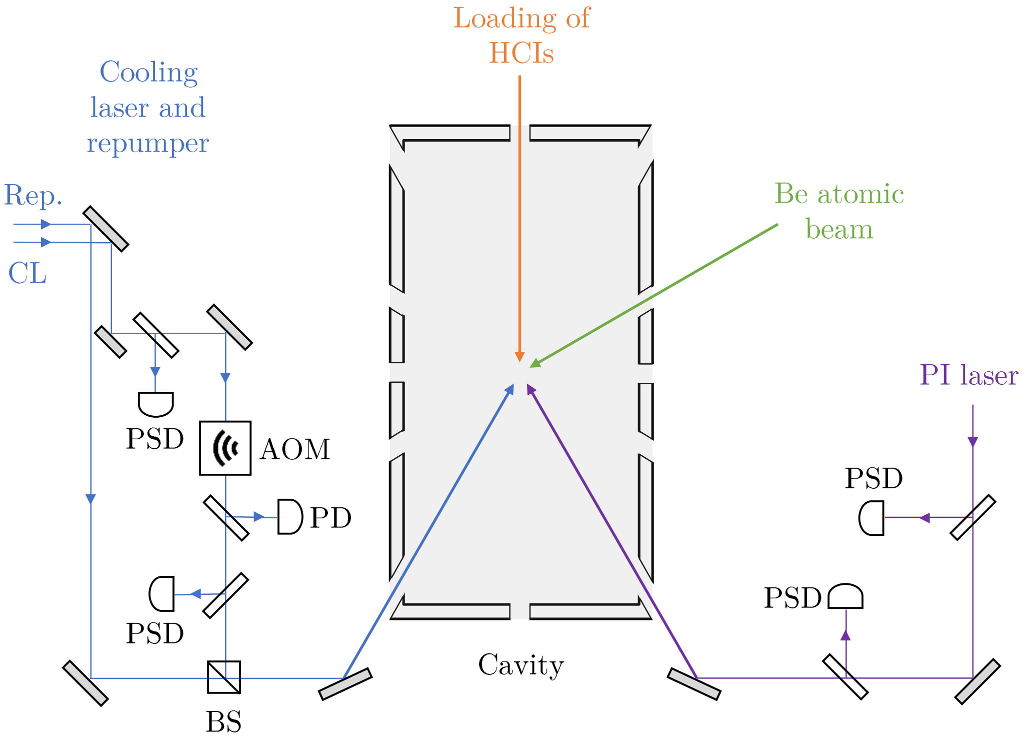
Loading of HCIs
Cooling laser and repumper
Rep.
CL
Be atomic beam
PI laser
PSD
AOM
PD
PSD
BS
Cavity
PSD
PSD

Figure 3.5: Schematic picture of the optical ports of the cavity and the laser setup around the trap. Two of the optical ports are for the loading of the ions. The HCIs are supplied by the beamline; the atomic beryllium beam is hit by the PI laser at an angle of 90° in the trap centre, through which Be^+ ions are produced. Both laser systems are position stabilised by piezo-driven mirrors (not pictured) onto the respective position-sensitive detector (PSD). The cooling laser power is stabilised by the AOM, through which it goes in $+1^{st}$ order, and the photodiode (PD). The repumper's frequency is adjusted by two AOMs that are not pictured here. The cooling laser and the repumper are overlapped with a beam splitter (BS) before they are guided into the trap.

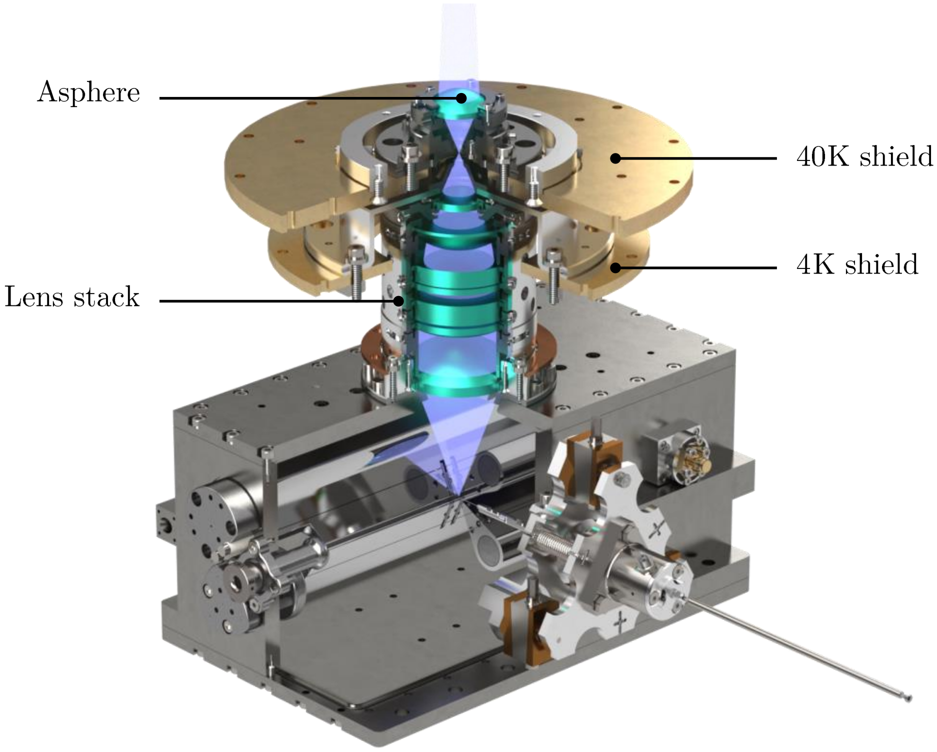

Figure 3.6: The fluorescence light from the Doppler cooling is used for imaging of the ions. Fluorescence photons are collected and focused with the lens stack on top of the cavity. A vertically adjustable ashpere can be used to change magnification. With adjustments taken from Ref. [31].

it on the detection systems installed above. The magnification can be adjusted by an asphere with adaptable distance from the lens stack.

A beam splitter divides the collected light, and sends half to an EMCCD (electron multiplying charge-coupled device) camera[2] and the other half to a photomultiplier tube[3] (PMT). The CCD camera is used for imaging the ions in the trap and for crystal diagnostics, as it provides spatially resolved information. The PMT is useful for investigating ion dynamics since it has a finer time-resolution.

---

[2] Andor iXon Ultra 888

[3] Hamamatsu H10682-210

4 Development and Testing of a Motorised Mirror Mount

Laser setups can be tricky and oftentimes require a significant amount of time aligning, realigning, and optimising beams by hand. In the case of CryPTEx-II the laser beams have to ultimately be guided through the optical trap access and the trap centre to interact with the trapped ion or ion crystal. Good alignment is essential, even more so when it comes to more advanced laser cooling systems, as described in Section 2.2.2, and can be less consistent when done by hand.

Computer-controlled mirror positioning has the potential to considerably improve the consistency of alignment. In the scope of this work, the development of such a mirror mount at a relatively low cost, that can be controlled remotely with motors, was carried out. The design and construction of such a motorised mirror mount (MMM) is described in Section 4.1, the first tests that have been performed are described in Section 4.2.

4.1 Design and Assembly

There are a few requirements that we need our home-built MMM to fulfill. The first is that we need the structure to be mechanically stable to ensure reproducible alignment and positioning. The second constraint we have is that we want this solution to be cost effective compared to commercial motorised installations that usually come at a significant cost. For this reason we decided to use commercially available, standardised stepper motors[1] and kinetic mirror mounts. The challenge thus lies in finding an effective way to connect these components.

While the simplest kinematic mirror mounts have their two adjustment screws, for horizontal and vertical adjustments, on the back of the mount for the circular mirror, we chose a mount with vertical adjustment screws[2]. This allows for two stepper motors, one for each adjustment screw, to be installed on top of the mount extending the structure vertically which will take up less space within a laser setup. A frame was designed that would enclose the mirror mount and where the motors could be secured from the top to sit directly above the adjustment screws.

The problem that is left to solve is the connection of the shafts of the motors to the adjustment screws of the mirror mount where the knobs were removed and replaced by

---

[1] NEMA 8

[2] Thorlabs VM1/M

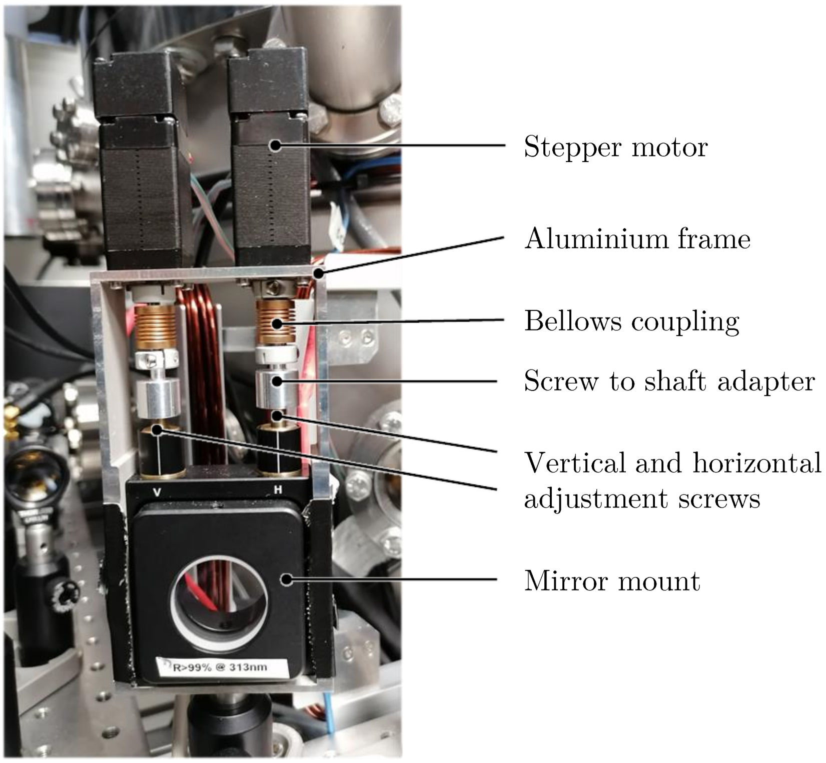
Stepper motor
Aluminium frame
Bellows coupling
Screw to shaft adapter
Vertical and horizontal adjustment screws
Mirror mount
V
H
R>99% @ 313nm

Figure 4.1: An assembled motorised mirror mount (MMM)

shafts similar to those of the motors. Here we run into the problem of the changing height if the screws are turned. To allow for this axial motion, a bellows coupling[3] was chosen to connect the two shafts. They allow an axial misalignment of $^{+0.4}_{-1.2}$ mm. The final device is pictured in Figure 4.1.

The motor power is supplied by the motor driver[4], that is additionally connected to the encoder which ensures correct translation from input signal to motor movement. Said input signal is sent from an Arduino that runs Grbl, an open-source G-code parser[5].

4.2 The First Test Setup

A small laser setup was assembled to test the performance of the new MMM. The setup included a helium-neon laser as a laser source and a CMOS camera[6] as a detector; a picture can be seen in Figure 4.2.

Neutral density (ND) Filters and a beam splitter were used to attenuate the beam

---

[3] GMT FACB12-4-4

[4] HBS57

[5] `https://github.com/grbl/grbl`

[6] DELOCK 96382

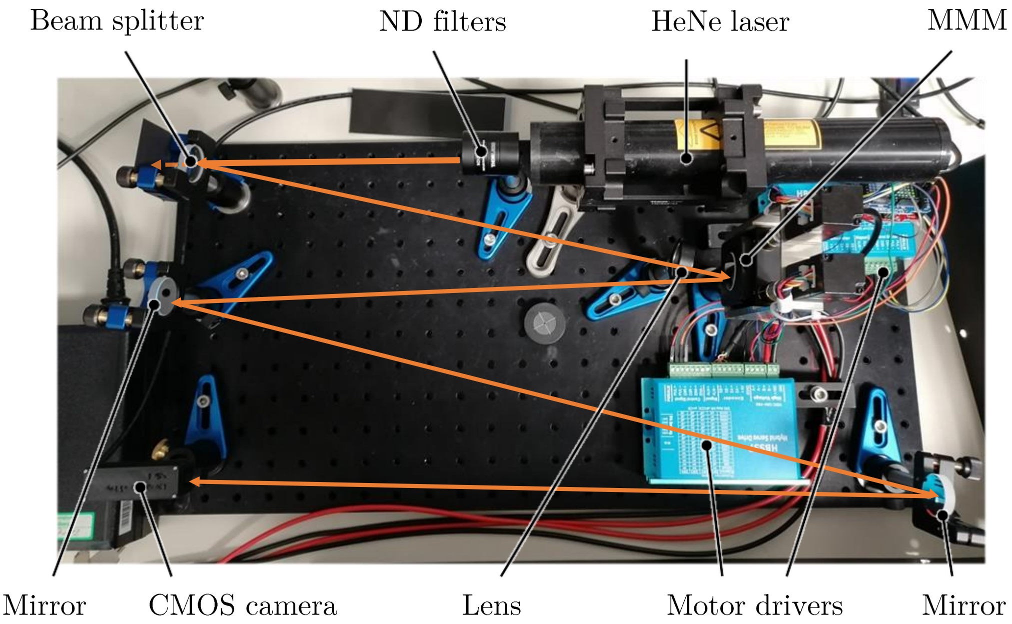

Figure 4.2: Test setup for the first operation of a home-built MMM, consisting of a HeNe laser, weakened by ND filters and a beam splitter, as a light source and a CMOS camera as a detector. The distance of the MMM to the detector was measured to be 105(2) cm.

in order to not damage the detector. The camera as it comes has a lens screwed in front of the detector that results in a fixed focus. Using it as is with the HeNe laser pointing directly at the camera we get optical artefacts from the lens in the picture (see Figure 4.3a) which hinder the evaluation of the laser position. Therefore, the camera lens was removed and the laser beam hits the detector directly in this setup. The resulting images from the camera are shown in Figure 4.3, where it is clear why the solution without the camera lens was chosen.

Two detection methods were tested for determining the laser position from the camera output. In both cases a Gaussian blur filter (once with an adjustable size blur, for the second with a blur size of 11) was applied to the greyscale image to reduce image noise. For the first option the brightest pixel in this resulting frame is taken as the laser position. In the second method a threshold mask is applied to the image and the weighted average of the pixel above the threshold is the determined position. Both options are fast enough to keep up with the frame rate of the camera.

In the following, the performance of the MMM and that of the two detection methods will be investigated. The two methods will be called maximum method and threshold method, respectively.

Firstly, decoupled horizontal (along the x axis on the detector) and vertical (along y axis) movements were supplied by the motors, one at a time, resulting in a rectangular

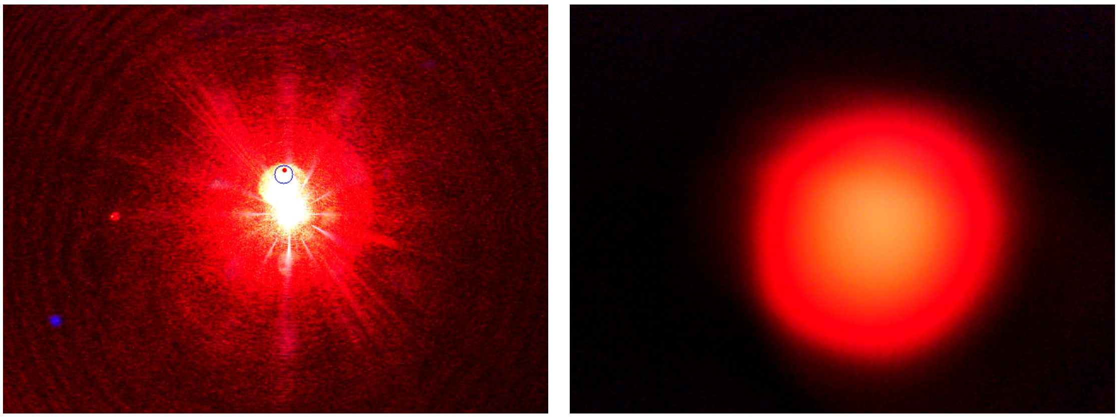
(a) (b)

Figure 4.3: Images taken by the CMOS camera that was used as a detector of the HeNe laser first **(a)** with the camera lens attached and then **(b)** without. The second picture corresponds to the setup that was used for the initial measurements presented here.

path of the laser beam. For each of the detection methods the determined laser position was saved and can be seen in Figure 4.4. The first observation we can immediately make from the two different paths is that the maximum method shows larger fluctuations compared to the same laser path observed with the threshold method, and might not be sufficient in determining the laser position.

The installed motors have a step size of 1.8° with a 5 % non-accumulative uncertainty. In the x direction the motor is turned by 112.5° here, resulting in a distance of about 424.8(14) px on the detector. Consequently, a single step of 1.8° corresponds to 6.8(3) px, or 38.2(19) µm on the camera sensor. With a distance between MMM and detector of 105(2) cm we can calculate that one motor step turns the mirror mount by

$$\sigma_{\text{motor step}} = 7.5(4)\,\text{arcsec}. \tag{4.1}$$

To roughly figure out the resolution of the detection methods, the deviation from the average x position along one of the vertical sides of the rectangle, where the x position was not changed with the motor, was determined. This average x value is also indicated in Figure 4.4.

For the two methods the standard deviation is

$$\Delta_{\text{maximum}} = 3.6\,\text{px}, \tag{4.2}$$

$$\Delta_{\text{threshold}} = 0.92\,\text{px}. \tag{4.3}$$

In two separate measurements, one motor's position was moved back and forth by the same value repeatedly, while the other was still. Simultaneously, the laser position

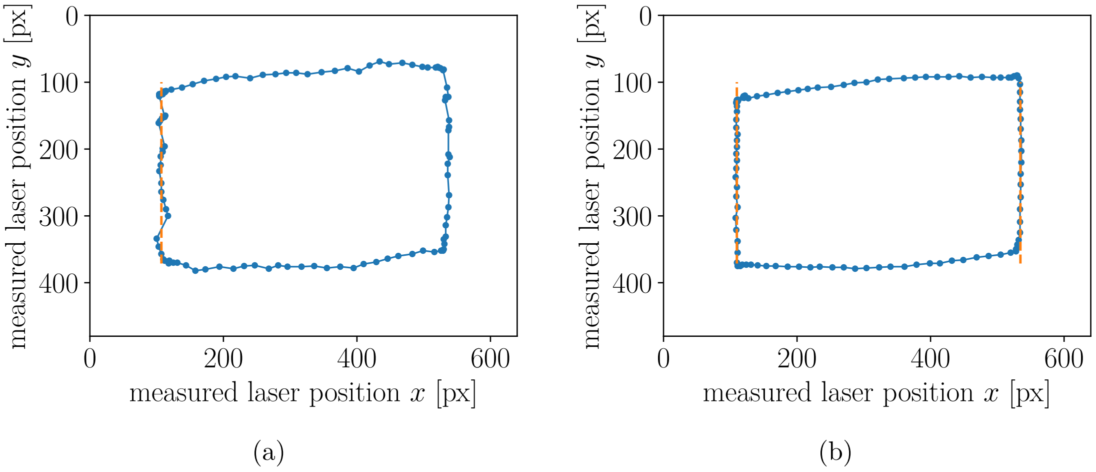

Figure 4.4: Laser position on camera for a rectangle, determined with **(a)** the maximum method, and **(b)** the threshold method. On the left (and also the right for the second picture) side of the rectangle, where the motor for the horizontal adjustment was not moved, the mean horizontal position is indicated in orange. The shape as is appears on the detector looks to entirely rectangular. This could be caused by the mechanical hysteresis that can be seen in Figure 4.5.

on the camera sensor was measured using the threshold method. The relevant laser position is shown against the time, which was determined from the number of frames with the framerate of 5 fps, see Figure 4.5. Shown as an overlay on the laser position is the corresponding motor position at the time.

For the horizontal movement we see an excellent agreement between laser beam position and motor position. The vertical movement looks less promising. The motor motion was similar to the previous measurement, but it does not fit the determined laser position. This seems to be caused by mechanical hysteresis.

As the MMM was assembled we noticed the vertical adjustment screw being looser in its thread than the horizontal one. Most likely there was not enough lubricating grease left on the screw and the thread after fixing the new knobs on the screws.

From the back and forth movement we also determine the velocity of the laser position. A simple linear fit to a linear part of the motion yields

$$v = 29.13(6)\,\mathrm{px\,s^{-1}} \mathrel{\widehat{=}} 32.2(6)\,\mathrm{arcsec\,s^{-1}}\,, \tag{4.4}$$

for the horizontal motion, and for the vertical motion

$$v = 29.0(4)\,\mathrm{px\,s^{-1}} \mathrel{\widehat{=}} 32.1(7)\,\mathrm{arcsec\,s^{-1}}\,. \tag{4.5}$$

These values for the speed of both mirror axes agree well with each other. Since the motor rotation speed was tuned to the same value and the laser path was adjusted as

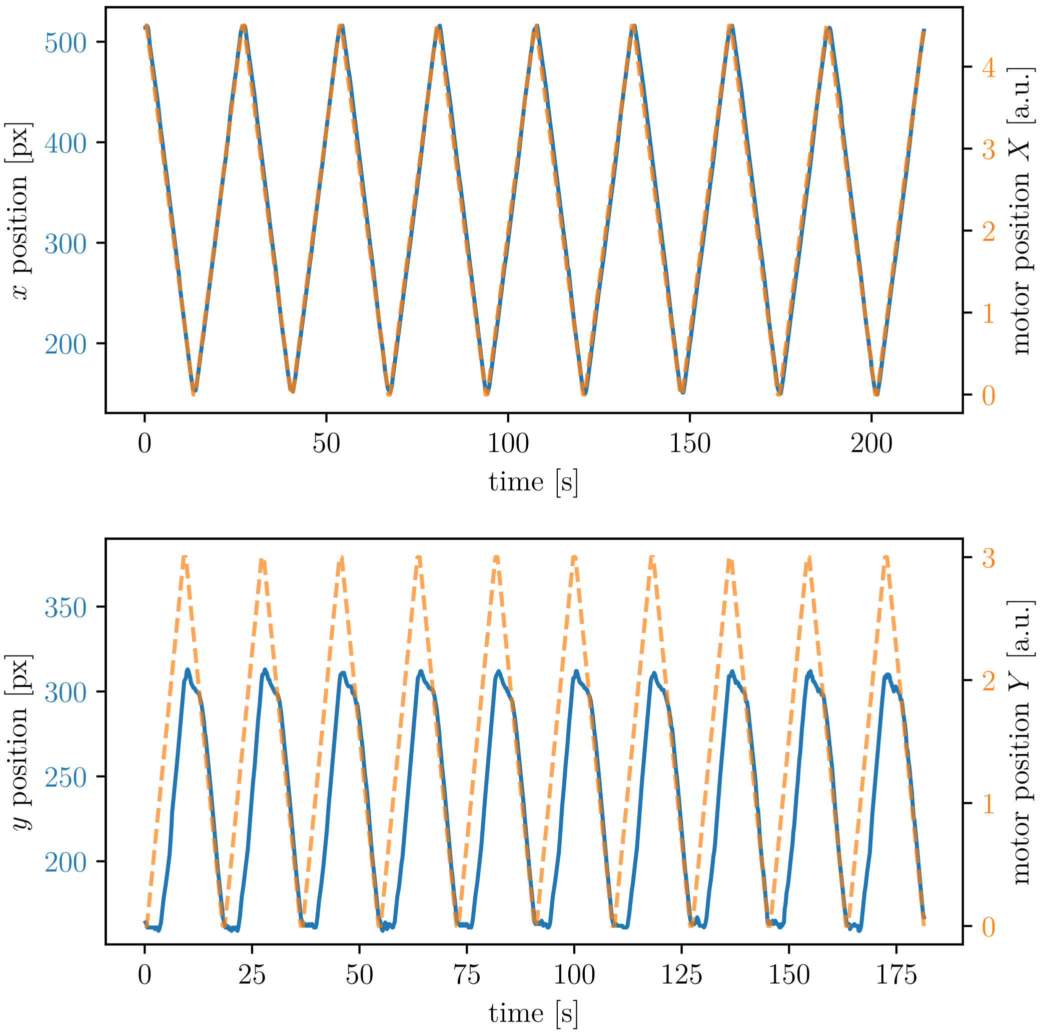

Figure 4.5: Measurements for both axes, where the adjusting motor was moved back and forth while the other motor was kept stationary, were done, shown is the relevant position on the detector (blue) and the corresponding motor position (orange) as a function of the time. The transfer of motor to mirror motion for the vertical adjustment screw shows mechanical hysteresis.

parallel as possible to the table, hitting the detector under an angle of close to zero, we can conclude that the translation from motor to mirror motion is the same for both axes.

It should be noted that the velocity of the motor was purposefully limited to a low value for the first test here, and faster velocities should be possible. During this testing the maximum motor rotation was limited to $7.5\,^\circ\,\mathrm{s}^{-1}$. With the earlier obtained conversion from the motor motion to the distance on the detector and hence to the angular adjustment to the mirror plane, this leads to $28.32(9)\,\mathrm{px\,s}^{-1}$, or $31.3(6)\,\mathrm{arcsec\,s}^{-1}$. This agrees with the velocity as it was determined from the detected laser beam movement (see 4.4, 4.5).

This first test demonstrates the successful operation of the home-built MMM system, including computer-controlled mirror alignment and detecting the corresponding movement of the laser spot. Its angular resolution was measured at 7.5(4) arcsec which corresponds to a single step of the motor.

Mechanical hysteresis was noted for one of the axes. This can hopefully be improved upon, if not fixed, in the future, since the other axis shows no significant signs of hysteresis. It appears to be an issue of the mirror mount that was used rather than a limitation of the MMM design. Other than this the motor motion of both axes gets equally converted into an adjustment of the mirror.

The next tests will include an increased rotation velocities to evaluate how fast the motor motion can be before something stops working in the translation of the motion. Additionally, we will be using the system of a MMM with the CMOS detector as a form of beam stabilising. While the speed will never reach those of a piezo controlled mirror at several (tenths of) kHz, it is well-suited for compensating slow drifts in laser pointing.

5 Characterisation of the Trap Parameters of CryPTEx-II

As seen in Chapter 2, the a and q values of a Paul trap are closely related to a trapped ion's motion, as they for instance determine the secular frequency of the macromotion. So by measuring the secular frequencies ω_u, with Equation (2.14) the a and q values can be calculated. The measurements were done with singly charged beryllium ions (Be^+) loaded into the trap. They can be carried out for a single particle in the trap as well as for a loaded ion crystal, as the secular frequency only depends on the charge-to-mass ratio. In the case of a crystal there are several more vibrational modes which could potentially be excited but the secular motion corresponds to the common motional mode. Since this mode consists of all ions moving together, it is the easiest to excite by any methods that couple to all ions equally.

5.1 Secular Motion Excitation

The secular motion correspond to motion in a harmonic oscillator potential so to measure the secular frequency we drive this harmonic oscillator with a sinusoidal force of varying frequency to find the resonance. For an undamped, or harmonic oscillator, which is assumed here, the resonant driving frequency is equal to the oscillator frequency, here the secular frequency. This is still the case for a weakly-damped harmonic oscillator, which is the case here, as seen from the ion movement, with a small resonance width compared to the frequency.

A few different sources for the driving force were attempted. An electric driving force was set with the mirror electrodes (seen in Figure 3.3). This was not strong enough to have an observable effect on the ion at the resonance, most likely due to the large distance of the mirror electrodes to the trap centre. The method that ended up visibly exciting the ions was adding a sinusoidal modification to the cooling laser power. With a function generator and the power stabilising AOM of the cooling laser this modification was added. As we have already seen in Section 2.2.1, the radiation force of a laser can have a significant impact on the the ion motion.

First, the frequency was scanned manually, and the image of the trapped ions was observed on the EMCCD camera showing their fluorescence light. At the resonances an apparent change of the ion shape on the camera is observed. Along the axis where the motion is driven the ion moves with an increased amplitude and fluorescence photons

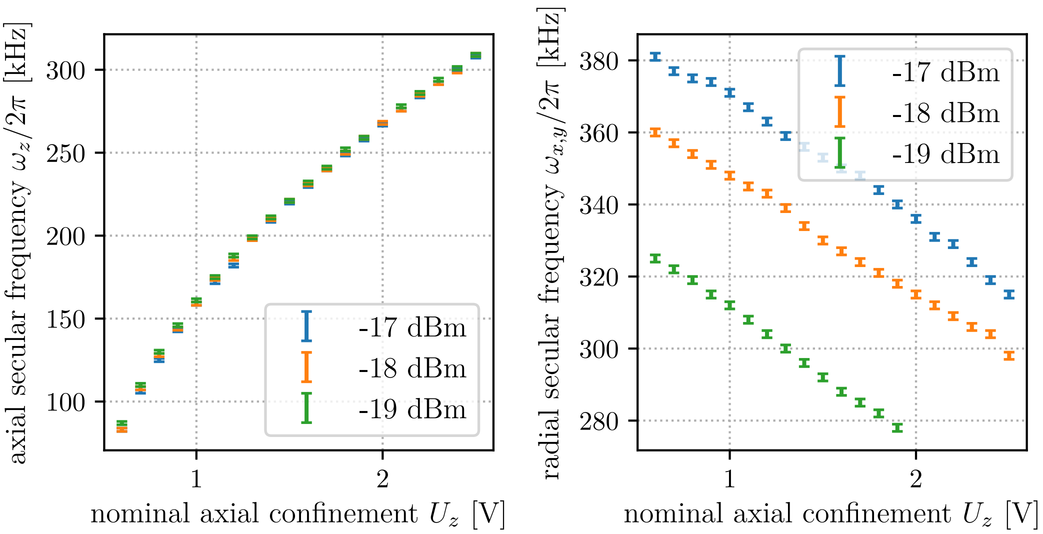

Figure 5.1: Values of the secular frequencies at different rf powers as a function of the axial confinement U_z as set by the external power supply. The values given for the rf power are the ones set on the function generator before further amplification. **Left:** Axial secular frequency, **Right:** Radial secular frequency.

are emitted at all points along this increased motion. This results in a smeared out apparent position of the ion on the CCD camera, as the ion motion is too fast for the time-resolution of the CCD. It looks like a line instead of a point, either in axial or radial direction depending on which secular motion is excited. The two radial directions are indistinguishable on the camera image.

For three different rf input powers to the resonator and thus the rf quadrupole field strengths, the axial and radial secular frequencies were measured while varying the axial confinement U_z. This data is pictured in Figure 5.1.

The rf signal is set by a signal generator[1] which is then amplified by 40 dB and the DC electrodes are connected to individual channels of computer-controlled digital-to-analog converters[2].

5.2 Axial Secular Motion

First we focus on the axial secular frequency. The data (pictured on the left hand side of Figure 5.1) shows no dependence on the rf power which is what we expect from the theory. The q value for the axial motion is zero (see Equation (2.10)), therefore the

---

[1] Rohde & Schwarz SMB100B

[2] National Instruments NI PCI-6703

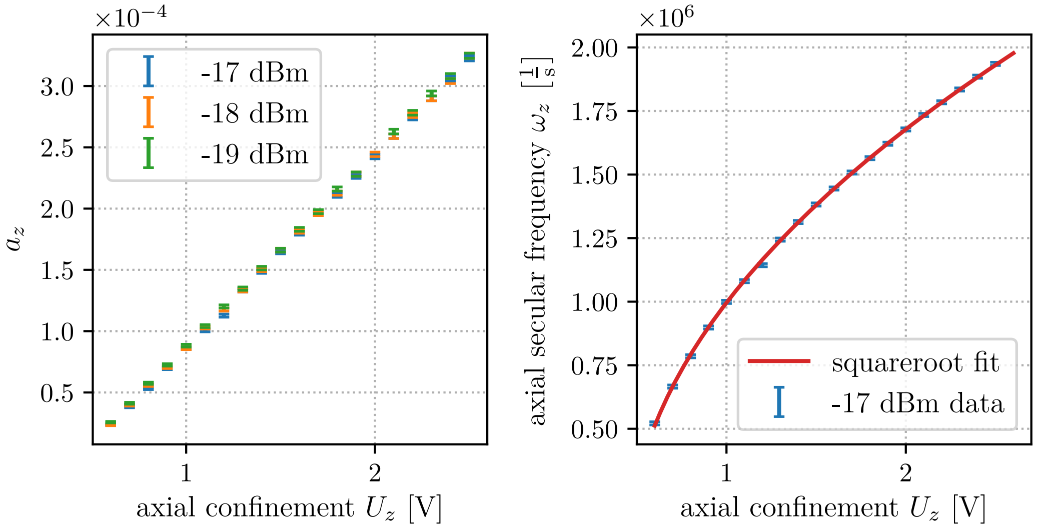

Figure 5.2: **Left:** a_z values calculated from the axial secular frequencies at different axial confinements and rf powers. **Right:** The axial secular frequency is plotted against the axial confinement for the measurement of $-17\,\mathrm{dBm}$ rf power. A fit of the form of Equation (5.2) is performed on this data to determine the geometrical factor κ; here shown is the result for one dataset, the ones for rf powers of $-18\,\mathrm{dBm}$ and $-19\,\mathrm{dBm}$ look very similar. For the resulting fit parameters see Table 5.1.

relation of a_z and axial secular frequency ω_z simplifies to

$$\omega_z = \frac{\Omega}{2}\sqrt{a_z}\,, \tag{5.1}$$

a_z only depending on the axial DC potential (see Equation (2.9)). The measured secular frequencies can be directly converted using the resonator frequency Ω and are pictured on the left hand side in Figure 5.2. It shows a linear dependency, as was expected from Equation (2.9).

From Equation (2.14) and Equations (2.9) and (2.10) we expect the following dependence on the axial potential:

$$\omega_z = \frac{\Omega}{2}\sqrt{\frac{8Q\kappa U_z}{m\Omega^2 z_0^2}} = \sqrt{\frac{2Q\kappa U_z}{m z_0^2}}\,. \tag{5.2}$$

Fitting this to the data lets us determine the geometrical factor κ. For the fit an offset to the voltage has to be introduced such that the actual fit function looks like

$$\omega_z = \sqrt{\frac{2Q\kappa\left(U_z - U_{\text{offset}}\right)}{m z_0^2}}\,, \tag{5.3}$$

Table 5.1: Fit parameters for the different fits to the axial frequency, like the one on the right hand side in Figure 5.2. The given uncertainties are the ones arising from the fitting, for which the uncertainties of the secular frequency was taken into account. The rf level listed here is read out before further amplification.

rf level [dBm]	κ	U_{offset} [V]
−19	0.3579(7)	0.4376(16)
−18	0.3578(7)	0.4494(16)
−17	0.3575(11)	0.4562(26)

with κ and U_{offset} as the fitting parameters. One of the fits is shown on the right hand side in Figure 5.2, since the other two fits look almost identical they are not also pictured. All the resulting fit parameters are given in Table 5.1.

The values for κ agree nicely with each other and the average is calculated to be

$$\kappa = 0.3578(5). \tag{5.4}$$

The offset to the applied voltage appears to be slightly dependent on the rf power and was therefore not averaged. We do not know the cause of this offset between the externally applied voltage and the apparent voltage in the trap centre as experienced by the trapped ions. Perhaps it is due to a voltage drop in the cabling somewhere, although this should not be possible since the resistance to ground of the electrode is essentially infinite. Whether it is related to the rf voltage is difficult to check since the measurements cannot be done without the rf signal.

Since the geometrical factor κ depends on the geometry of the DC electrodes, it can also be determined from a simulation of the potential in the trap, in particular along the trap axis. Simulated was the static potential on the trap axis for all DC electrodes being set to 1 V [41], the simulation results are pictured in Figure 5.3.

On the trap axis the only potential one expects is the harmonic potential

$$\phi(z) = \frac{\kappa U_z}{z_0^2}\, z^2, \tag{5.5}$$

as all other terms in Equations (2.1) and (2.5) vanish for $x = 0$ and $y = 0$.

By fitting the parabolic part of the potential around the trap centre, also displayed in Figure 5.3, the geometrical factor is here determined to be

$$\kappa_{\text{sim}} = 0.337\,75(10) \tag{5.6}$$

The κ value given in Ref. [31], also determined from simulations, where additional higher orders were included in the fit polynomial, is $\kappa \approx 0.3379$. It is in very good agreement

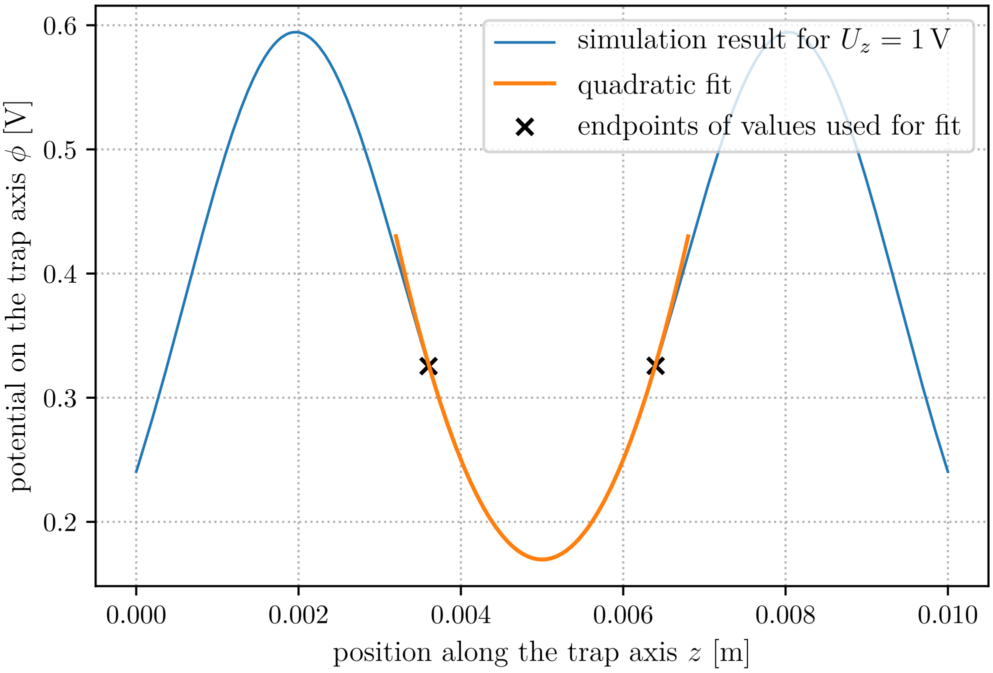

Figure 5.3: Simulated potential along the trap axis where $x = y = 0$ for all the DC electrodes set to $1\,\mathrm{V}$. The harmonic potential close to the centre, located at z = 0.005 m in this simulation, was fitted with a quadratic fit to find the geometrical factor κ (see Equation (5.5)). The region that was fitted is the one between the endpoints indicated in black.

with the value determined from the simulation here, which is not very surprising as a very similar analysis was done.

The values for κ from the simulations are not in good agreement with the values determined from the secular frequencies. The error margins on the simulation values do not take any manufacturing tolerances into account, although this probably would not be enough to account for the difference. The general dependence of the axial frequency on the axial confinement voltage still matches the expectations, and as seen in Figure 5.2 on the right the fit seems quite good.

The discrepancy between the values therefore has to be explained by a systematic effect not considered in the simulations. Additionally, an offset had to be introduced to describe the data, which was not expected.

5.3 Radial Secular Motion

For the same values of axial confinement where the axial frequency was measured, the radial secular frequency was also noted. But since neither $a_{x,y}$, nor $q_{x,y}$ vanish here (see Equations (2.9) and (2.10)), the radial secular frequency depends on both static axial confinement strength U_z and rf amplitude V.

Besides the dependence on the axial confinement U_z, $a_{x,y}$ also depend on an additional static x/y quadrupole, if present, in Section 2.1 denoted with U_r. It breaks the degeneracy between the values of a_x and a_y and therefore also to two different frequencies ω_x and ω_y. The resonator electrodes should not have a static quadrupole component, but with the DC electrodes such a U_r can be introduced. This DC setting — the mean voltage difference between the four DC electrodes within the x quadrupole electrode and the other four within the y quadrupole electrode — will be called the radial confinement balance. For the measurements in Figure 5.1 it was nominally set to 0, but to investigate the relation of the radial confinement balance to the static quadrupole as experienced by the ions, a scan of the radial secular frequencies at different radial confinement balances was done. As seen in Figure 5.4, at a radial confinement balance of zero there are two radial secular frequencies observed, meaning a non-vanishing static quardupole acts on the ions.

To see a how the DC settings for the radial balance translate to the static quadrupole offset experienced by the ions in the trap, a simultaneous fit of the form

$$\omega_{x,y} = \frac{\Omega}{2}\sqrt{\frac{4Q}{m\Omega^2}\left(\pm\frac{2\xi(U_r - \widetilde{U}_{\text{offset}})}{r_0^2} - \frac{\kappa(U_z - U_{\text{offset}})}{z_0^2}\right) + \frac{1}{2}\left(\frac{4QV}{mr_0^2\Omega^2}\right)^2} \tag{5.7}$$

of the two radial frequencies was done. A new geometrical factor ξ and voltage offset $\widetilde{U}_{\text{offset}}$ are introduced as fit-parameters to describe the translation from the DC setting to the effective change in the trap centre, and as a third parameter V yields the rf amplitude experienced by the ions. The values for κ and U_{offset} are adopted as they were determined in the previous part about the axial motion (see Table 5.1).

The resulting fit, seen in Figure 5.4, can explain the data around the relevant part between the crossing of the frequencies and the low U_r values. It also give us the first estimate of the effective rf potential as

$$V = 97.38(14)\,\text{V}, \tag{5.8}$$

at an rf level of −18 dBm (before amplification). As the fit was not ideal this uncertainty given here is not necessarily a good representation.

We still assume that we can use this fit to characterise the radial potential offset with

$$\begin{aligned} \xi &= 0.0281(6), \\ \widetilde{U}_{\text{offset}} &= -1.67(8)\,\text{V}, \end{aligned} \tag{5.9}$$

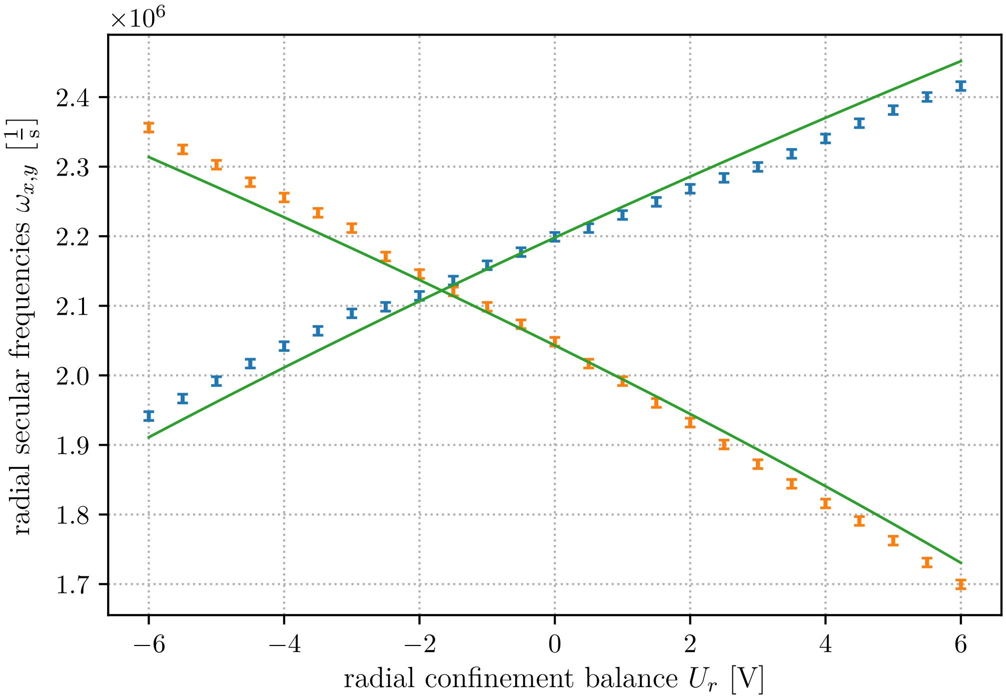

Figure 5.4: The two radial secular frequencies ω_x (in blue) and ω_y (in orange) as a function of the applied radial confinement balance U_r which adds a static offset to the x/y quadrupole potential. The data for both secular frequencies was simultaneously fitted to find the geometrical factor ξ and the voltage offset describing the effect of the voltage setting on the radial confinement as experienced by trapped ions. The data was taken at a non-amplified rf power of $-18\,\mathrm{dBm}$.

as we took our earlier measurements at $U_r = 0$ where the fit is a reasonable description.

To investigate the radial potential, that is the radial q values and the rf amplitude, with the data in Figure 5.1, we need take into account the non-vanishing static quadrupole at zero nominal radial confinement balance, at which the measurements were performed, due to the offset $\widetilde{U}_{\text{offset}}$. This also means that there was a second radial frequency, like in Figure 5.4 at $U_r = 0$, however, that resonance was not found at the time and was therefore not measured. Ideally, it would have led to the same $q_{x,y}$ values and the same rf amplitude V, but for now this cannot be checked.

We will come back the data of Fig. 5.1 and first continue by analyzing a measurement series where both radial frequencies were determined.

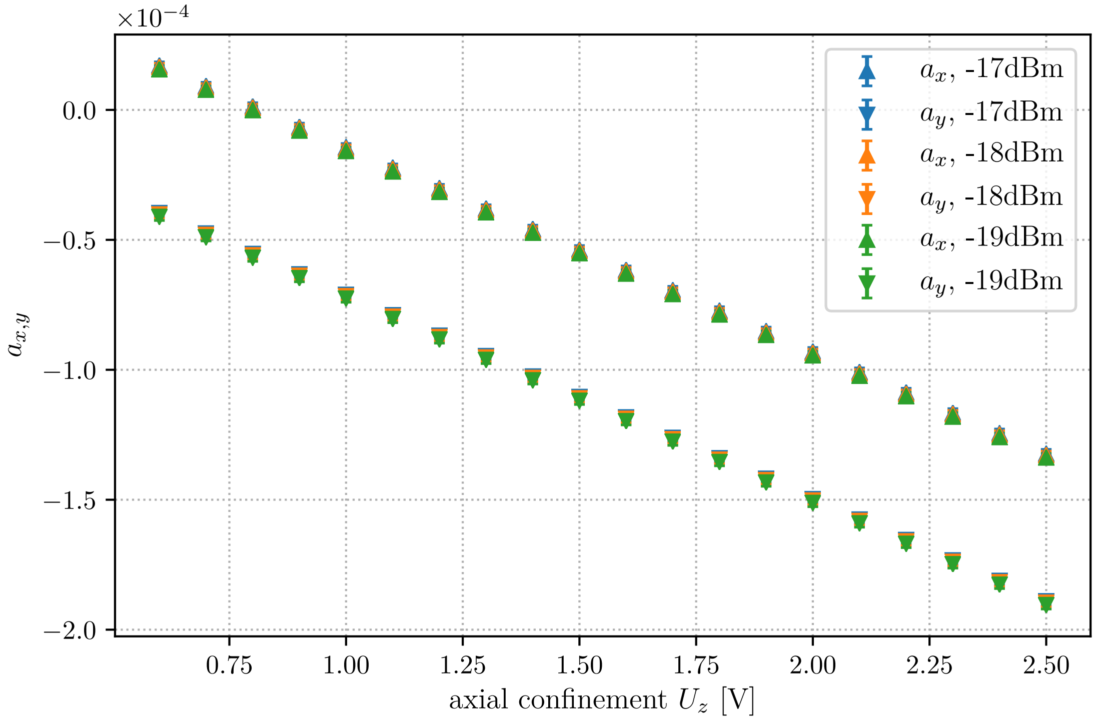

Figure 5.5: The a_x and a_y values as a function of axial confinement U_z, calculated from the DC voltage settings with Equation (5.10). As the offsets U_{offset} and $\widetilde{U}_{\text{offset}}$ were used in the calculation, the U_z values shown are the nominal ones.

From the voltage settings, the values for a_x and a_y were determined with

$$a_{x,y} = \frac{4Q}{m\Omega^2}\left(\pm\frac{2\xi(U_r - \widetilde{U}_{\text{offset}})}{r_0^2} - \frac{\kappa(U_z - U_{\text{offset}})}{z_0^2}\right), \tag{5.10}$$

adjusted from Equation (2.9), and pictured in Figure 5.5. The resulting radial a values are very small at an order of 10^{-4} which indicates that the adiabatic approximation for the motion in the Paul trap is appropriate (see Equation (2.12)). With Equation (2.14) rearranged to

$$q_{x,y} = \mp 2\sqrt{\left(\frac{2\omega_{x,y}}{\Omega}\right)^2 - a_{x,y}}\,, \tag{5.11}$$

the $a_{x,y}$ values and the measured secular frequencies lead to the $q_{x,y}$ values. Comparing the radial frequency measured earlier (right hand side of Figure 5.1) with the data for the changing radial confinement balance (Figure 5.4), we see that of the two possible radial frequencies we had measured the lower one, corresponding to the lower a_u value, here a_y.

The calculated q_y values are shown in Figure 5.6. It shows that the q_y value is not significantly dependent on the axial confinement, which is to be expected from

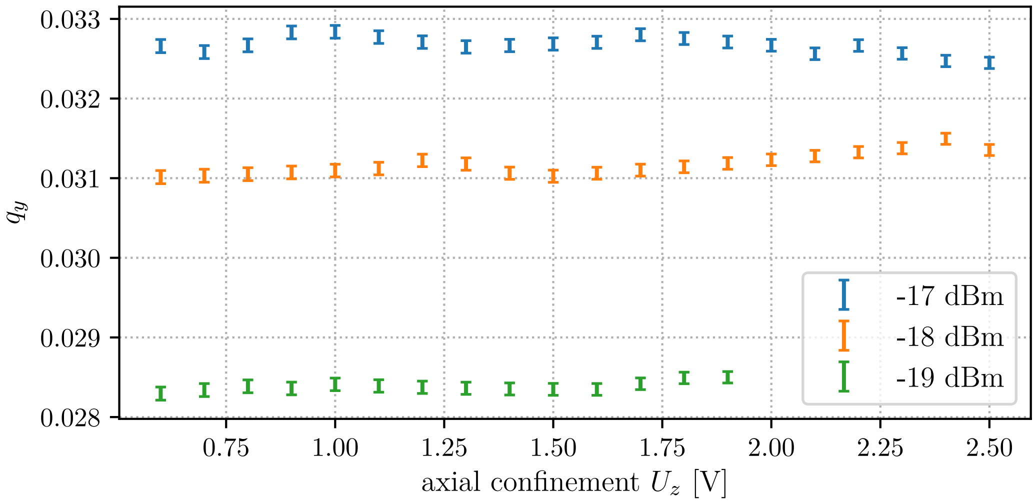

Figure 5.6: $q_y = -q_x$ calculated from the measured radial secular frequencies and the calculated a_y values. It shows only a dependence on the rf power and not on the axial confinement, as was expected.

Equation (2.10). With Equation (2.10) the rf amplitude V can be calculated as well shown as a function of the pickup voltage (Figure 5.7). This is the voltage picked up by a weakly coupled capacitive coupler in the resonator which should be proportional to the actual rf field strength. The final averaged q_y values and voltages at the different examined rf levels are presented in Table 5.2.

The resulting relation pictured in Figure 5.7 is indeed roughly linear and fitted with a line. The conversion from the pickup (peak-peak) voltage $V_{\text{pickup, pp}}$ is therefore determined to be

$$V = 810(16) \times V_{\text{pickup, pp}}. \tag{5.12}$$

This allows us to have a measure of the rf amplitude that can be read out in the lab.

Table 5.2: Results for the analysis of the radial secular frequencies, the q factors and the effective rf voltage amplitude V at different rf levels were determined.

rf level [dBm]	pickup voltage [mV$_{\text{pp}}$]	$q_y = -q_x$	rf amplitude V [V]
−19	114(1)	0.028 38(9)	94.12(19)
−18	127(1)	0.031 17(15)	103.4(4)
−17	140(1)	0.032 67(13)	108.3(3)

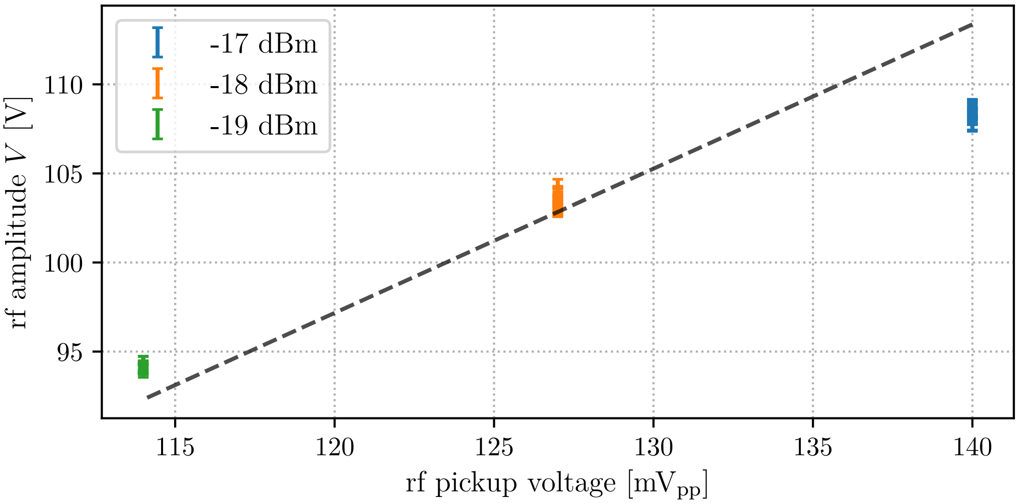

Figure 5.7: Calculated from the different q_y values, the rf amplitude V as it is experienced by trapped ions at different rf powers, pictured as a function of the rf pickup voltage. A linear fit without an offset was done to get the conversion from the readout pickup voltage to the rf amplitude V.

6 Cooling Laser Profile in the Trap Centre

A first application of the new home-built MMM is a measurement of the beam profile and in particular the beam width of the Doppler cooling laser in the trap centre. During the initial construction of CryPTEx-II the beam width was approximated by measuring it outside the vacuum chamber at a distance that equaled the position of the trap centre. The $1/e^2$ width of the cooling laser and the repumper was determined as 340 µm and 310 µm, respectively [31]. With the use of the new MMM the actual beam width at the ion position was investigated by using the fluorescence light of the ions that indicates the intensity of the laser light.

How the laser setup was modified to include the MMM is described in the following Section 6.1. Afterwards the calibration of camera readout to in-trap position and the measurements of the laser beam profile are described in Section 6.2 and Section 6.3, respectively.

6.1 Incorporation of the MMM Into the Cooling Laser Setup

The MMM was installed in the cooling laser setup right before the beam enters the vacuum chamber and the camera on the opposite side where the beam exits. This allowed the laser position behind the trap and the fluorescence light of a loaded ion (or ion crystal) to be observed coincidentally. The setup can be seen in Figure 6.1.

The camera is the same CMOS detector used in the test setup of Section 4.2, but here we run into the problem that it cannot detect UV light. So instead of removing the focusing lens as before and having the laser shine directly onto the sensor, a different solution has to be found. What was used is the fact that UV light causes a visible fluorescence of blue wavelengths on bleached paper. A screen with a top layer of white paper was placed in the laser beam path and the camera was set up next to the optical opening and pointed towards the screen. The focusing lens in front of the detector was not removed.

In Section 4.1 we saw that the better and more reliable method for determining the beam position was the one using a mask with a certain pixel brightness threshold. This method still works with this new setup and was therefore still used here. In this method the result can not only be given in exact integer pixels, but the average of the detected region can give the result in fractions of pixels. This was not necessary in the HeNe setup, but was integral to the determination of the exact laser position here as the full range of laser beam movement on the camera image is far smaller.

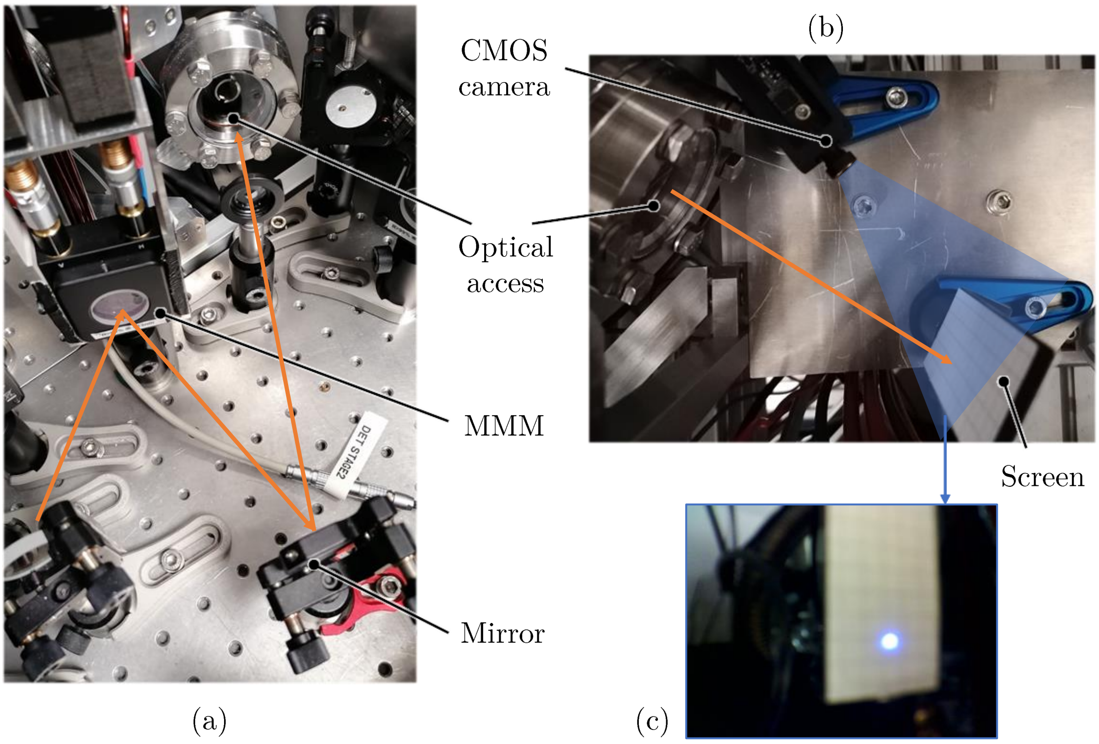

Figure 6.1: **(a)** The MMM was installed in the laser setup as the second to last mirror before cooling laser and repumper enter the cavity. The path of cooling laser and repumper is shown in orange. **(b)** Behind the trap the laser beams (indicated in orange) exit the trap and hit a screen. The CMOS camera, with its lens attached, is pointed at this screen. **(c)** A picture taken with the CMOS camera while the laser, and the room light, was turned on. The blue fluorescence light of the UV laser hitting the paper on the screen, from which the position was determined, can be seen.

The correlation between the motor position, as translated by the input G-code, and the laser beam position, as seen by the camera, is found to be nearly linear (see Figure 6.2). Hence, this new detection method for the beam position is reliable and we can go forwards with the cooling beam measurements.

For the vertical axis there are still remnants of the mechanical hysteresis effects we already noted in Section 4.2.

6.2 Calibration Using the DC Potential

For the calibration of the laser position behind the trap to its position in the trap centre we use the DC potential of the Paul trap to shift the ions along the trap axis. This also

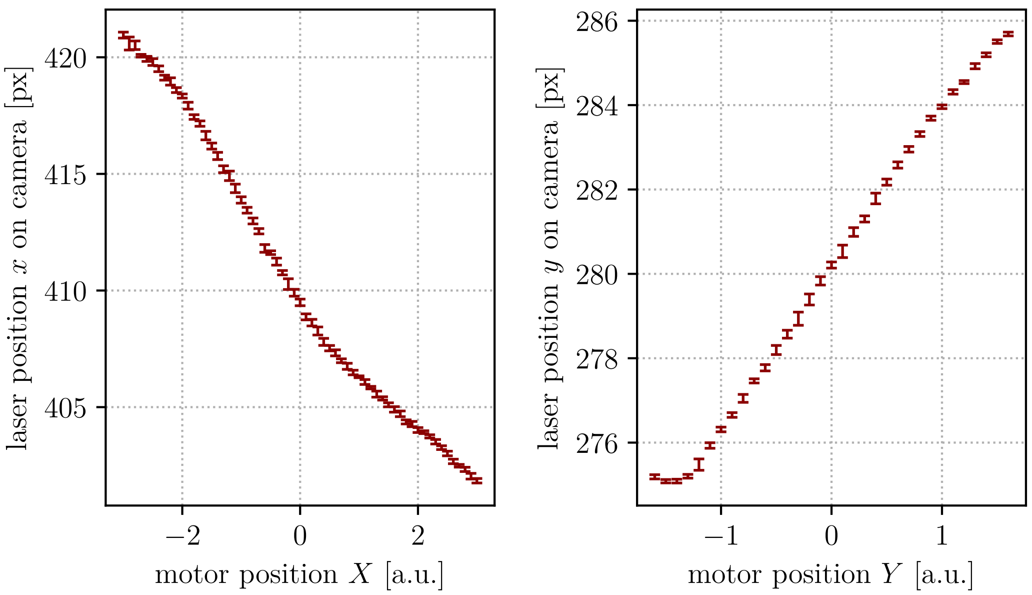

Figure 6.2: Shown is the laser position determined by the camera pointing at the screen behind the trap centre as a function of the motor position, **Left:** for the horizontal mirror axis, **Right:** for the vertical axis.

moves them out of the focus of the cooling laser which has an angle of 30° to the trap axis, and the hence the fluorescence goes down. We then realign the cooling laser onto the ion(s) with the MMM and save the laser position the camera observes.

As seen before in Section 3.1 there are eight DC electrodes in the Paul trap to confine the ions along the z direction. They produce a potential minimum between them. Typically they are set on the same value on each side to create a minimum right in the centre between them but as as we introduce an offset that we add to the 4 electrodes at positive z and subtract from the DC electrodes at negative z, the position of the minimum shifts along the trap axis. The ions will be located at this minimum and therefore will move out of the cooling laser beam.

The way the position of the minimum shifts with a certain offset is derived by a simulation of the produced potential using COMSOL [41]. The simulated potentials on the beam axis for different voltages of the electrodes are shown in Figure 6.3.

The minima can be plotted against the offset and a linear fit gives us a conversion from said offset to axial position. This is shown in Figure 6.4. As the cooling laser meets the trap axis under an angle of $\alpha = 30°$ the difference in position orthogonal to the laser, x, is

$$x = d\,\sin(\alpha) = \frac{d}{2}, \tag{6.1}$$

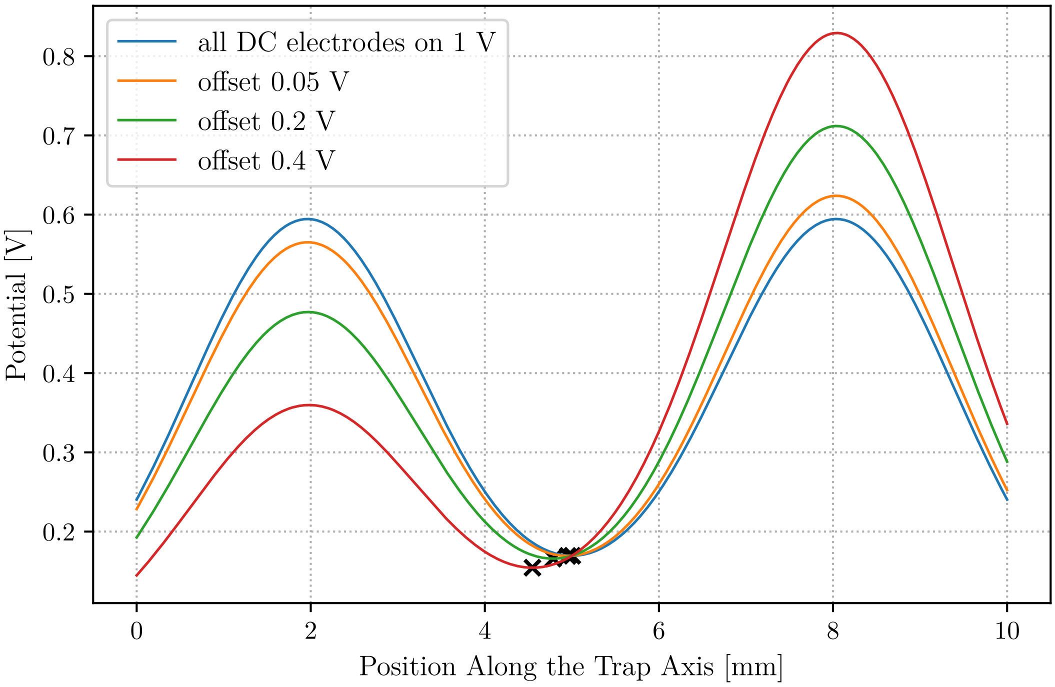

Figure 6.3: Result of simulations of the potential along the trap axis for different voltage offsets. The two sets of four DC electrodes are set to $1.0\,\mathrm{V} \pm$ offset. The simulations were done with COMSOL. The minima, where the ion in the trap will be found, are marked in black.

for a difference in the ion position d. In Figure 6.4 the positions of the minima have already been corrected for this. The conversion from the fit is

$$x\,[\mathrm{mm}] = 0.573(9) \cdot \Delta\varphi\,[\mathrm{V}] - 0.0021(21). \tag{6.2}$$

The uncertainties shown here are purely from the linear fit.

After introducing an offset to the trapping potential the MMM is used to realign the cooling laser to the highest possible ion fluorescence as seen on the EMCCD camera. We save the corresponding laser position determined with the CMOS camera. Two series of calibration measurements were done, after some mirrors for the cooling laser had to be readjusted by hand in-between measurements. The next section will go into details about the measurements and will point out where the different calibrations are used.

The plots of the laser position in pixels versus the axial distance from the trap centre are seen in Figure 6.5, the applied offset was converted with Equation (6.2). Again a linear fit was utilised to get the conversion, this time between the pixel value of the laser position and the corresponding orthogonal displacement of the laser focus in the trap centre. The quantity of interest is then the distance in the trap, w, that two different

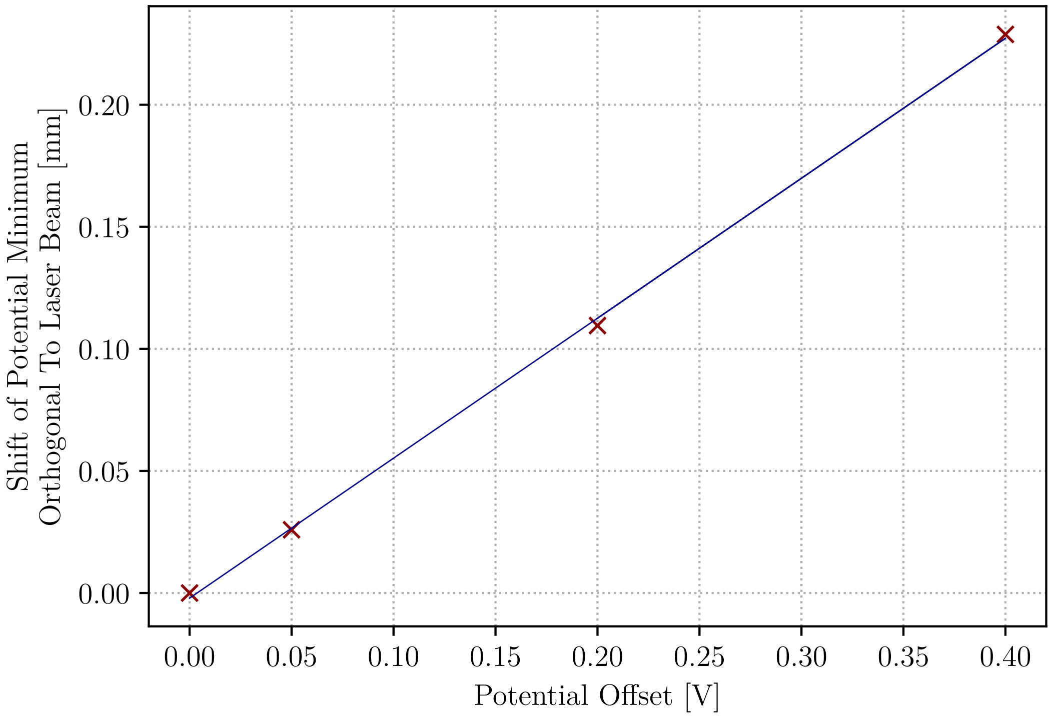

Figure 6.4: From the simulations in Figure 6.3 we get the shift of the potential minimum as a function of the potential offset applied to the electrodes, which is plotted here. A linear fit is done.

laser positions behind the trap, px_1 and px_2, correspond to. We get the following from the fit in Figure 6.5:

$$w = 0.0702(25)\,\mathrm{mm}\,(\mathrm{px}_1 - \mathrm{px}_2) \tag{6.3}$$

for the first calibration, and

$$w = 0.044(3)\,\mathrm{mm}\,(\mathrm{px}_1 - \mathrm{px}_2) \tag{6.4}$$

for the second calibration.

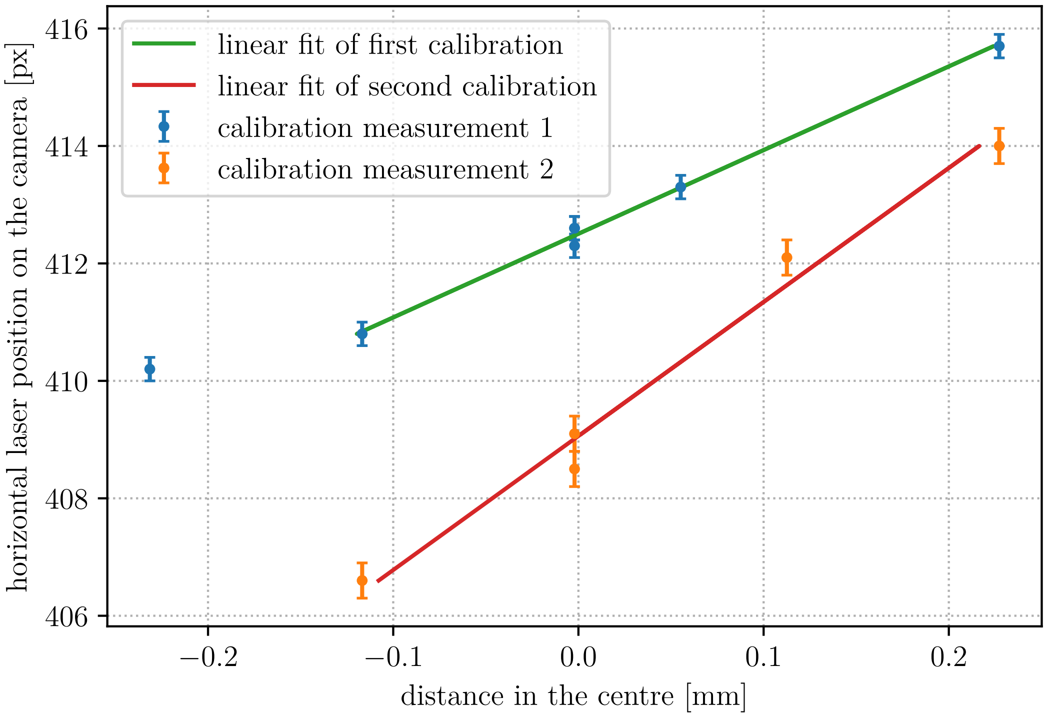

Figure 6.5: Results of the calibration of the movement of the laser focus in the trap versus the position of the laser spot measured behind the trap. On the horizontal axis is the shift of the laser focus from the trap centre calculated from the result of the fit seen in Figure 6.4 and corrected for the laser beam axis. A fit was done to obtain the conversion between the detected laser position and the distance in the centre. One of the values from the first calibration was excluded from the fit as the alignment of the laser for these voltage settings was not very successful due to too much stray light. The first calibration was done with two ions in the trap; for the second calibration there was one ion.

6.3 Beam Width Measurements

Knowing which laser position correspond to what displacement of the focus in the trap centre, we make a scan over the width of the laser profile. Around the point with the highest counts on the EMCCD camera a horizontal and a vertical sweep was done while simultaneously the fluorescence of the ion or ion crystal, as well as the laser position, was monitored.

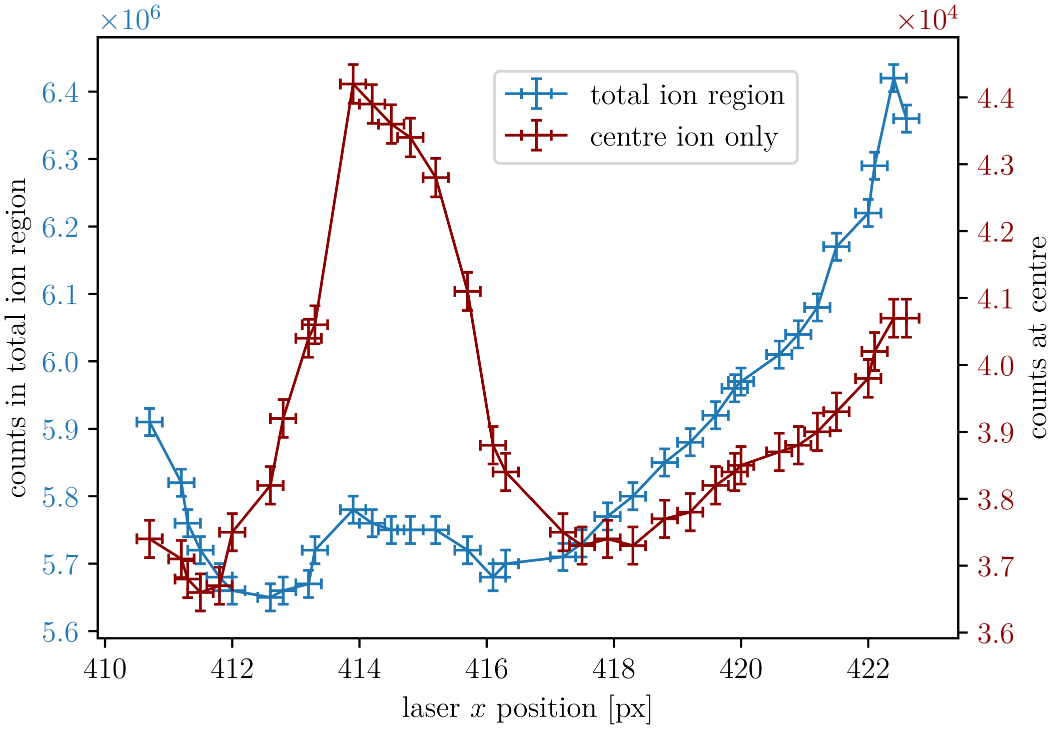

Figure 6.6: Counts on the EMCCD for different laser positions along the horizontal plane. Considered were two different regions of interest, the counts for which are shown in different colours. The counts shown in red are from a region that is very tight around the ion while the second region in blue is wider and includes reflections of the grid below the lens stack.

6.3.1 Measurements with the EMCCD camera

At first a preliminary measurement was taken using the EMCCD camera. This was mainly to test the measurement principle and get a feel for how the MMM, the CMOS laser detection and the fluorescence measurement work together.

This measurement was done while there was a single ion trapped. The EMCCD camera was turned to video acquisition and two regions of interest were defined in the camera picture. One enclosing only the ion in the centre and a second larger region that includes the halo of fluorescence light caused by the grid structure in the resonator on top of which the lens stack sits. Here a horizontal sweep was done, after the vertical position with the highest counts was determined.

The data in Figure 6.6 shows a central peak from the fluorescence light and increased stray light if one goes too far in either direction. We can see that the counts over the larger region don't show a clear or useful fluorescence signal and so for this first measurement

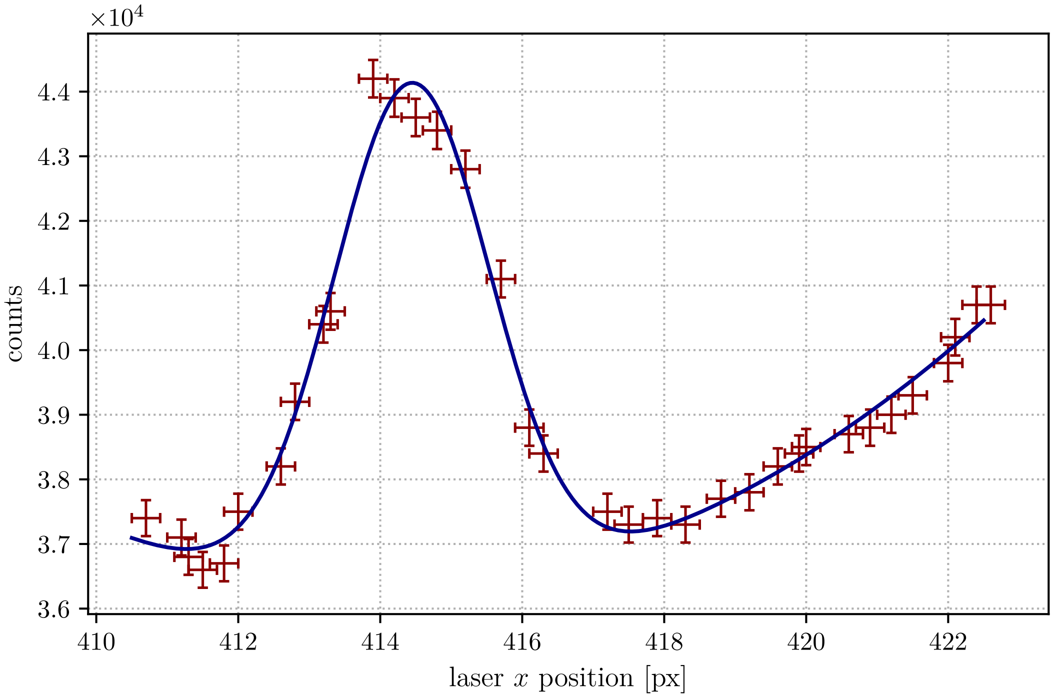

Figure 6.7: The counts for the ion as given by the EMCCD camera are fitted to obtain the width of the fluorescence peak and therefore the width of the cooling laser beam in the trap centre. The fit function is the sum of a Gaussian and a quadratic polynomial. The quadratic function is used to approximate the background of the stray light and the Gaussian yields the variance used to derive the $1/e^2$ width.

the counts that were used to determine the width of the laser beam were the ones from only the smaller region around the visible ion. For this we define a fit function in an attempt to extract the beam width from the data. The background with the stay light is approximated with a quadratic function and we add this to the Gaussian that we use to fit the peak of the fluorescence peak. The resulting fit is shown in Figure 6.7.

Next to the FWHM, another standard measure of a laser beam width is the $1/e^2$ radius, that describes the distance from the centre of the beam where the intensity has decreased to $1/e^2 = 13.5\,\%$ of the maximum. For a Gaussian this equals twice its standard deviation σ. The width of the beam is twice the radius and therefore 4σ, comparatively the FWHM corresponds to $2\sqrt{2\ln 2}\,\sigma$. From the Gaussian in the fit we obtain

$$\sigma = 1.11(4)\,\text{px}, \tag{6.5}$$

which results in a FWHM and a $1/e^2$ width w of

$$\begin{aligned} \text{FWHM} &= 183(9)\,\mu\text{m} \\ w &= 312(16)\,\mu\text{m} \end{aligned} \tag{6.6}$$

For this the conversion from the first calibration was used.

Compared to the expected value for the cooling laser width of 340 µm, the value appears to be slightly smaller. However, it agrees with the value previously measured for the repumper. Since ions only fluoresce when they interact with both cooling laser and repumper, we can argue that with the new detection method we observe the profile of where the two laser beams overlap. A $1/e^2$ width agreeing with the smaller repumper width would therefore be consistent with a good (horizontal) overlap of both beams in the trap centre.

6.3.2 Measurements with the PMT

After the first working example, where the fluorescence was studied with the EMCCD camera, measurements were taken with the PMT. The workflow for these measurements was automated to get the laser position and the PMT readout over a certain region of motor positions. A larger number of ions increases the amount of fluorescence light so to increase the signal-to-noise ratio more than one ion was loaded into the trap. Here the measurements were taken with an initial Coulomb crystal of 4 ions.

For a one dimensional sweep again the EMCCD camera was used to find the laser position that would yield the highest counts as best as possible along one axis and then a scan was carried out along the other. The data can be seen in Figure 6.8. We can see that the horizontal scan has less stray light compared to the signal and will most likely allow for a better and more accurate result for the width of the laser beam.

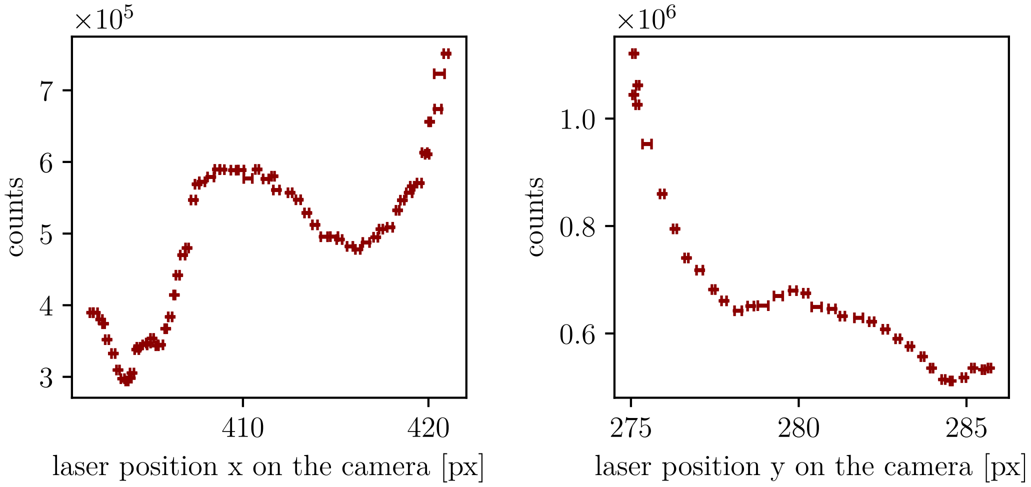

Figure 6.8: PMT counts as a function of the laser position behind the trap. Two scans were done, **Left:** counts for the horizontal scan over the x position of the laser, and **Right:** counts of the vertical scan as a function of the y position of the laser. Both show areas with a significant amount of stray light.

Table 6.1: Cooling laser width as determined from the peaks of the PMT measurement after subtracting a linear background.

scan direction	FWHM [µm]	$1/e^2$ width [µm]
horizontal scan	251(21)	345(25)
vertical scan	188(16)	247(18)

However, while the laser beam itself is expected to have a Gaussian profile, this cannot be seen in either PMT measurement and the simple fit of a Gaussian function will not result in an accurate value for the width. This implies a non-linear dependence of the fluorescence on the laser intensity, most likely caused by the saturation of the cooling transition. Instead, a different method has to be used. As most fit functions that were tried could not describe the data well, the background of the peak itself was estimated to be linear and subtracted, and the FWHM and the $1/e^2$ width were determined from the resulting peak.

This evaluation can be seen in Figure 6.9 and the results are given in Table 6.1. For the uncertainties of the determined widths, the uncertainties of the laser position on the camera was taken into consideration, but they are dominated by the uncertainty from the calibration.

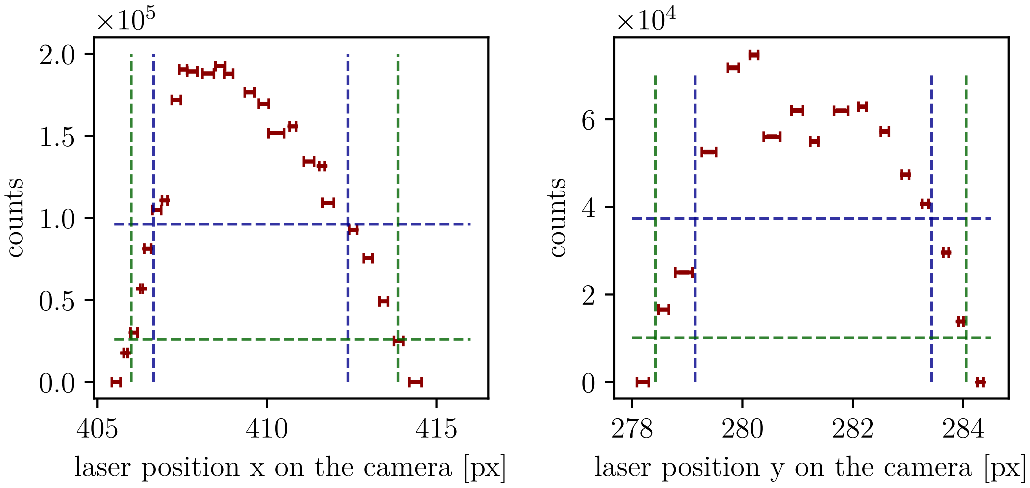

Figure 6.9: From the data shown in Figure 6.8 the background of the peaks is subtracted linearly and the resulting peaks are shown here. The FWHM and the $1/e^2$ width were determined from the decrease of the counts compared to the maximum value. **Left:** Peak from the horizontal scan, **right:** peak from the vertical scan.

The measurements with the EMCCD and PMT were conducted on different days and readjustment of the cooling laser path was necessary to reduce the stray light enough to get a good enough fluorescence signal with the PMT. For the readjustment the last two mirrors of the laser setup were tuned, the MMM and a standard mirror mount adjusted by hand. For this reason the calibration measurement was redone as mentioned before and the second calibration is used for the PMT measurement.

The cooling laser width determined from the horizontal scan agrees within 1.1 σ with the value determined with the EMCCD counts. For the vertical scan the width was determined to be significantly smaller. While it is possible that the beam profile is not perfectly circular, it is also possible that the laser beam was not in the ideal horizontal position, also suggested from the smaller peak compared to the horizontal scan. It should also be kept in mind that the conversion from camera position in pixels, to the position in the trap was established from only a horizontal calibration. This could have an impact on the value from the vertical scan in comparison to the ones from the horizontal scan.

For a better description of the background an additional scan over the trap centre could be done without loading any ions. Should this measurement be repeated, the background determined this way could be subtracted from the data to get more accurate fluorescence peaks.

An additional 2D scan was done in an attempt to get an idea of the whole beam profile of the laser beam. The result is shown in Figure 6.10.The beam profile indeed does not resemble a circle and is more elliptical. This could be the case because either the beam profiles of the two lasers is already not circular, or the overlap of the two beams is slightly misaligned in the trap centre.

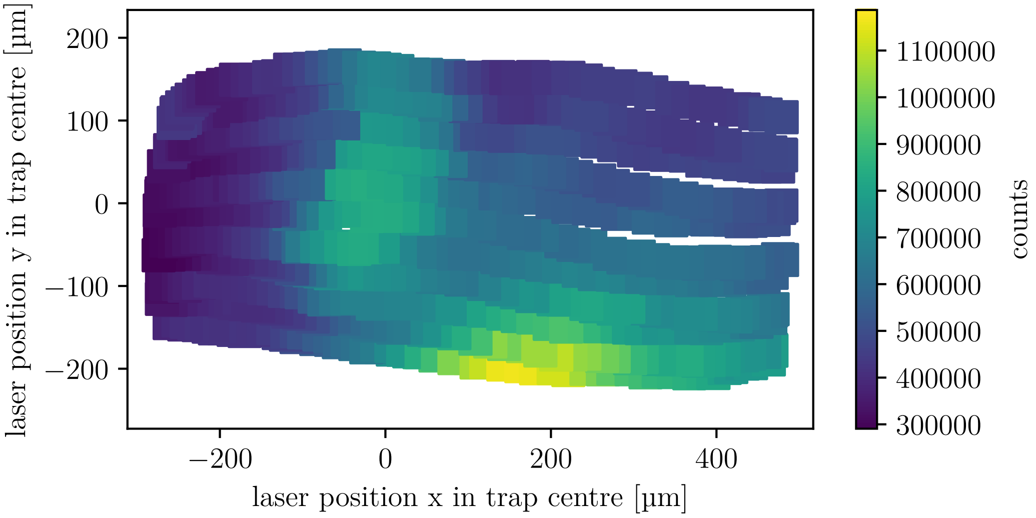

Figure 6.10: A 2D scan over the cooling laser profile was done. The PMT counts at different laser positions as determined by the CMOS camera behind the trap are pictured. The bright spot on the bottom edge of the image is stray light. The elliptical shape on the left hand side of the image was due to fluorescence light of the ions, this should resemble the beam profile of the cooling laser.

7 Conclusion and outlook

The aim of this thesis was the characterisation of the ion motion in the linear Paul trap at the heart of CryPTEx-II, as well as the characterisation of the cooling laser used for Doppler cooling singly charged beryllium ions in the trap. A motorised mirror mount (MMM) was constructed and tested in this work to help with the latter, and to overall improve the reproducible adjustment and stabilisation of the laser setup.

The MMM that was designed and constructed as a part of the work for this thesis is built around a commercially available mirror mount. Two stepper motors were connected to the adjustment screws for vertical and horizontal orientation of the mirror mount and are remotely controlled with an Arduino running a G-code parser.

The first test setup for the MMM, using a HeNe laser as a light source and a CMOS camera for detection of the laser spot position, let us determine the angular resolution as $\sigma = 7.5(4)\,\mathrm{arcsec}$. The adjustment speed, which was limited to $31.3(6)\,\mathrm{arcsec\,s^{-1}}$, can be increased in the future in further tests. During the testing, mechanical hysteresis was noted for one of the two adjustment screws of the mirror mount used. This seems to be the case because the one screw is less well greased in its thread, possibly from cleaning it to glue on the screw-to-shaft adapters. To fix this in this the screws could be re-greased once more, otherwise a different mirror mount could be used.

As a future application of the MMM, it will be used as beam stabilisation against slow drifts of the laser beam. This is already in the works and should yield the first results soon.

The cost-effective MMM design and camera detector can then be broadly used in any experimental setup where computer-controlled laser beam positioning or a compensation of slow drifts of laser beam pointing is needed.

For the characterisation of the ion motion in the linear Paul trap, the secular frequencies were excited in trapped beryllium ions with a modulation on the cooling laser power and noted for several (rf and DC) voltage settings. The axial and radial motion were evaluated separately.

The axial motion is only characterised by the axial confinement. From the set DC voltages and the axial frequencies the geometrical factor κ could be determined to be 0.3578(5), from simulations of the axial potential it was expected to be 0.337 75(10). The values don't quite agree with each other, but the fit to the data determining this κ seems to be a good description of the axial frequencies and thus of what axial potential is experienced by the ions. An unexpected voltage offset between the externally applied and the true voltage in the trap centre was observed. Further investigation is needed to find its origin.

The radial secular frequencies are dependent on the rf amplitude, as well as the voltage applied to the DC electrodes. If the trapped ions experience a static offset to the x/y quadrupole, then the degeneracy of a_x and a_y, and consequently the one of ω_x and ω_y, is lifted. With the DC electrodes such a static quadrupole offset can be introduced with the radial confinement balance.

With a scan over different DC settings changing the radial confinement balance, the (nominal) U_r value for a vanishing static quadrupole at the trap centre could be determined as $-1.67(8)\,\mathrm{V}$. Here the radial secular frequencies are degenerate.

The a_x and a_y values were calculated from the DC voltage settings and were determined to be of the order of 10^{-4}, which is quite small, as expected. From the measured radial secular frequency ω_y at different axial confinement strengths, and from the calculated a_y value, the q_y value was calculated and found to be at around 0.03. The determined radial a and q values suggest that the adiabatic approximation is a good estimate for the ion motion in the trap. From q_y the rf amplitude in the trap centre that acts on the ions could be determined and a conversion from the pickup voltage values, which can be read out in the laboratory, can be given as $V_{\mathrm{rf}} = 810(16) \times V_{\mathrm{pickup,\ pp}}$.

In addition to the motion of the ions in the trap, the 313 nm laser cooling beam profile was also characterised as a part of this work. The newly constructed MMM was used for these measurements. It was integrated into the cooling laser setup as the second to last mirror before the laser light was guided through the trap and the CMOS camera was used for position detection behind the trap.

To calibrate the laser position on the detector to the corresponding position in the trap centre, the axial potential minimum was moved while coincidentally observing the laser position for the highest fluorescence.

For the determination of the beam profile the laser beam was moved across the ions while the laser position and the fluorescence were monitored. In a first measurement the fluorescence was observed with the EMCCD camera and in ensuing measurements with the PMT. From the EMCCD data the $1/e^2$ width of the beam could be extracted from a Gaussian fit as 312(16) µm. The PMT data could not be successfully fitted, the width was taken at the point where the counts had declined by $1/e^2$ compared to the peak. This results in 345(25) µm for the horizontal direction and 247(18) µm for the vertical width. While it is possible that the cooling laser has less of a circular shape and is more elliptical, this could also indicate that the cooling laser and the repumper are not perfectly overlapped, since we expect a beam diameter of about 340 µm and 310 µm based on previous measurements for cooling laser and repumper, respectively. Fluorescence light is only visible if the ions are hit by the repumper as well as the cooling laser.

A 2D scan over the laser beam profile was done and showed an elliptical beam profile. If the elliptical profile is not (just) due to less than ideal overlapping of cooling laser and repumper it could also be an artifact of the astigmatism that the laser has after frequency doubling that was not perfectly corrected. The beam profile measurement could be repeated after changing the focusing optics of the 313 nm laser beams to optimise the beam size and shape.

Having the MMM and the CMOS camera for the detection of the laser beam position installed in the cooling laser setup already allows us to restore the laser beam paths more reliably than before. Installing a second MMM would give full computer-control over the beams and could be used to optimize the beams for minimum stray light.

Bibliography

[1] G. Kirchhoff and R. Bunsen, "Chemische analyse durch spectralbeobachtungen," *Annalen der Physik*, vol. 189, no. 7, pp. 337–381, 1861.

[2] T. H. Maiman, "Stimulated optical radiation in ruby," *Nature*, vol. 187, pp. 493–494, 1960.

[3] C. Wieman and T. W. Hänsch, "Doppler-free laser polarization spectroscopy," *Phys. Rev. Lett.*, vol. 36, pp. 1170–1173, May 1976.

[4] T. W. Hänsch, A. L. Schawlow, and G. W. Series, "The spectrum of atomic hydrogen," *Scientific American*, vol. 240, no. 3, pp. 94–111, 1979.

[5] W. Neuhauser, M. Hohenstatt, P. Toschek, and H. Dehmelt, "Optical-sideband cooling of visible atom cloud confined in parabolic well," *Phys. Rev. Lett.*, vol. 41, pp. 233–236, Jul 1978.

[6] D. J. Wineland and W. M. Itano, "Laser cooling of atoms," *Phys. Rev. A*, vol. 20, pp. 1521–1540, Oct 1979.

[7] T. Udem, R. Holzwarth, and T. W. Hänsch, "Optical frequency metrology," *Nature*, vol. 416, pp. 233–237, 2002.

[8] N. Huntemann, C. Sanner, B. Lipphardt, C. Tamm, and E. Peik, "Single-ion atomic clock with 3×10^{-18} systematic uncertainty," *Phys. Rev. Lett.*, vol. 116, p. 063001, Feb 2016.

[9] S. M. Brewer, J.-S. Chen, A. M. Hankin, E. R. Clements, C. W. Chou, D. J. Wineland, D. B. Hume, and D. R. Leibrandt, "^{27}al^{+} quantum-logic clock with a systematic uncertainty below 10^{-18}," *Phys. Rev. Lett.*, vol. 123, p. 033201, Jul 2019.

[10] C. A. Baker, D. D. Doyle, P. Geltenbort, K. Green, M. G. D. van der Grinten, P. G. Harris, P. Iaydjiev, S. N. Ivanov, D. J. R. May, J. M. Pendlebury, J. D. Richardson, D. Shiers, and K. F. Smith, "Improved experimental limit on the electric dipole moment of the neutron," *Phys. Rev. Lett.*, vol. 97, p. 131801, Sep 2006.

[11] S. Sturm, F. Köhler, J. Zatorski, A. Wagner, Z. Harman, G. Werth, W. Quint, C. H. Keitel, and K. Blaum, "High-precision measurement of the atomic mass of the electron," *Nature*, vol. 506, pp. 467–470, 2014.

[12] V. A. Dzuba, V. V. Flambaum, M. S. Safronova, S. G. Porsev, T. Pruttivarasin, M. A. Hohensee, and H. Häffner, "Strongly enhanced effects of lorentz symmetry violation in entangled yb+ ions," *Nature Physics*, vol. 12, pp. 465–468, 2016.

[13] R. M. Godun, P. B. R. Nisbet-Jones, J. M. Jones, S. A. King, L. A. M. Johnson, H. S. Margolis, K. Szymaniec, S. N. Lea, K. Bongs, and P. Gill, “Frequency ratio of two optical clock transitions in $^{171}\mathrm{yb}^{+}$ and constraints on the time variation of fundamental constants,” *Phys. Rev. Lett.*, vol. 113, p. 210801, Nov 2014.

[14] J. K. Webb, J. A. King, M. T. Murphy, V. V. Flambaum, R. F. Carswell, and M. B. Bainbridge, “Indications of a spatial variation of the fine structure constant,” *Phys. Rev. Lett.*, vol. 107, p. 191101, Oct 2011.

[15] M. G. Kozlov, M. S. Safronova, J. R. Crespo López-Urrutia, and P. O. Schmidt, “Highly charged ions: Optical clocks and applications in fundamental physics,” *Rev. Mod. Phys.*, vol. 90, p. 045005, Dec 2018.

[16] F. Currell, *The Physics of Multiply and Highly Charged Ions.* Springer Netherlands, 1 ed., 2003.

[17] P. Micke, T. Leopold, S. A. King, E. Benkler, L. J. Spieß, L. Schmöger, M. Schwarz, J. R. Crespo López-Urrutia, and P. O. Schmidt, “Coherent laser spectroscopy of highly charged ions using quantum logic,” *Nature*, vol. 578, pp. 60–65, 2020.

[18] L. Schmöger, *Kalte hochgeladene Ionen für Frequenzmetrologie.* PhD thesis, Ruprecht-Karls-Universität Heidelberg, 2017.

[19] A. D. Ludlow, M. M. Boyd, J. Ye, E. Peik, and P. O. Schmidt, “Optical atomic clocks,” *Rev. Mod. Phys.*, vol. 87, pp. 637–701, Jun 2015.

[20] R. Weinstock, “On a fallacious proof of earnshaw’s theorem,” *American Journal of Physics*, vol. 44, no. 4, pp. 392–393, 1976.

[21] L. S. Brown and G. Gabrielse, “Geonium theory: Physics of a single electron or ion in a penning trap,” *Rev. Mod. Phys.*, vol. 58, pp. 233–311, Jan 1986.

[22] W. Paul, “Electromagnetic traps for charged and neutral particles,” *Rev. Mod. Phys.*, vol. 62, pp. 531–540, Jul 1990.

[23] W. Paul and H. Steinwedel, “Notizen: Ein neues Massenspektrometer ohne Magnetfeld,” *Zeitschrift Naturforschung Teil A*, vol. 8, pp. 448–450, July 1953.

[24] K. Blaum, “Stored charged particles.” Lecture Notes, 2020/21.

[25] N. W. McLachlan, *Theory and Application of Mathieu-Functions.* Oxford: Clarendon-Press, 1947.

[26] D. J. Berkeland, J. D. Miller, J. C. Bergquist, W. M. Itano, and D. J. Wineland, “Minimization of ion micromotion in a paul trap,” *Journal of Applied Physics*, vol. 83, no. 10, pp. 5025–5033, 1998.

[27] J. Stark, “Design ultrastabiler hochfrequenzfelder für die langzeitspeicherung hochgeladener ionen,” Master’s thesis, Ruprecht-Karls-Universität Heidelberg, 2015.

[28] E. L. Raab, M. Prentiss, A. Cable, S. Chu, and D. E. Pritchard, “Trapping of neutral sodium atoms with radiation pressure,” *Phys. Rev. Lett.*, vol. 59, pp. 2631–2634,

Dec 1987.

[29] M. Marciante, C. Champenois, A. Calisti, J. Pedregosa-Gutierrez, and M. Knoop, "Ion dynamics in a linear radio-frequency trap with a single cooling laser," *Phys. Rev. A*, vol. 82, p. 033406, Sep 2010.

[30] D. Leibfried, R. Blatt, C. Monroe, and D. Wineland, "Quantum dynamics of single trapped ions," *Rev. Mod. Phys.*, vol. 75, pp. 281–324, Mar 2003.

[31] J. Stark, *An ultralow-noise superconducting radio-frequency ion trap for frequency metrology with highly charged ions.* PhD thesis, Ruprecht-Karls-Universität Heidelberg, 2020.

[32] S. Stenholm, "The semiclassical theory of laser cooling," *Rev. Mod. Phys.*, vol. 58, pp. 699–739, Jul 1986.

[33] D. J. Larson, J. C. Bergquist, J. J. Bollinger, W. M. Itano, and D. J. Wineland, "Sympathetic cooling of trapped ions: A laser-cooled two-species nonneutral ion plasma," *Phys. Rev. Lett.*, vol. 57, pp. 70–73, Jul 1986.

[34] M. Schwarz, O. O. Versolato, A. Windberger, F. R. Brunner, T. Ballance, S. N. Eberle, J. Ullrich, P. O. Schmidt, A. K. Hansen, A. D. Gingell, M. Drewsen, and J. R. C. López-Urrutia, "Cryogenic linear paul trap for cold highly charged ion experiments," *Review of Scientific Instruments*, vol. 83, no. 8, p. 083115, 2012.

[35] C. Fischer, G. Fuchs, B. Holzapfel, B. Schüpp-Niewa, and H. Warlimont, *Superconductors*, pp. 695–754. Berlin, Heidelberg: Springer Berlin Heidelberg, 2005.

[36] P. Micke, J. Stark, S. A. King, T. Leopold, T. Pfeifer, L. Schmöger, M. Schwarz, L. J. Spieß, P. O. Schmidt, and J. R. Crespo López-Urrutia, "Closed-cycle, low-vibration 4 k cryostat for ion traps and other applications," *Review of Scientific Instruments*, vol. 90, no. 6, p. 065104, 2019.

[37] A. Kramida, Yu. Ralchenko, J. Reader, and NIST ASD Team. NIST Atomic Spectra Database (ver. 5.8), [Online]. Available: `https://physics.nist.gov/asd` [2021, June 27]. National Institute of Standards and Technology, Gaithersburg, MD., 2020.

[38] H.-Y. Lo, J. Alonso, D. Kienzler, B. C. Keitch, L. E. de Clercq, V. Negnevitsky, and J. P. Home, "All-solid-state continuous-wave laser systems for ionization, cooling and quantum state manipulation of beryllium ions," *Applied Physics B*, vol. 114, pp. 17–25, 2014.

[39] A. E. Kramida, "Critical compilation of wavelengths and energy levels of singly ionized beryllium (be II)," *Physica Scripta*, vol. 72, pp. 309–319, Jan 2005.

[40] C. Warnecke, "Imaging of coulomb crystals in a cryogenic paul trap experiment," Master's thesis, Ruprecht-Karls-Universität Heidelberg, 2019.

[41] COMSOL simulations by Julian Stark, 2021.

Erklärung

Ich versichere, dass ich diese Arbeit selbstständig verfasst und keine anderen als die angegebenen Quellen und Hilfsmittel benutzt habe.

Heidelberg, den 9.7.2021, CVolk